AGU PUBLICATIONS

JGR

Journal of Geophysical Research: Atmospheres

RESEARCH ARTICLE
10.1002/2016JD025142

Key Points:
- Microphysical differences between storms with and without lightning activity occurred in all cloud layers
- Storms with lightning showed strong positive K_{DP} in the mixed one layer and negative K_{DP} in the glaciated layer
- Larger Z_H, Z_{DR}, and K_{DP} values in the warm layer were observed in storms with lightning activity

Correspondence to:
E.V. Mattos,
enrique.vmattos@gmail.com

Citation:
Mattos, E. V., L. A. T. Machado, E. R. Williams, and R. I. Albrecht (2016), Polarimetric radar characteristics of storms with and without lightning activity, *J. Geophys. Res. Atmos.*, *121*, 14,201–14,220, doi:10.1002/2016JD025142.

Received 24 MAR 2016
Accepted 14 NOV 2016
Accepted article online 17 NOV 2016
Published online 10 DEC 2016

Polarimetric radar characteristics of storms with and without lightning activity

Enrique V. Mattos[1], Luiz A. T. Machado[1], Earle R. Williams[2], and Rachel I. Albrecht[3]

[1]Instituto Nacional de Pesquisas Espaciais, Centro de Previsão de Tempo e Estudos Climáticos, Cachoeira Paulista, São Paulo, Brazil, [2]Massachusetts Institute of Technology, Parsons Laboratory, Cambridge, Massachusetts, USA, [3]Universidade de São Paulo, Instituto de Astronomia, Geofísica e Ciências Atmosféricas, Departamento de Ciências Atmosféricas, São Paulo, São Paulo, Brazil

Abstract This paper analyzes the cloud microphysics in different layers of storms as a function of three-dimensional total lightning density. A mobile X-band polarimetric radar and very high frequency (VHF) sources from Lightning Mapping Array (LMA) observations during the 2011/2012 Brazil spring-summer were used to determine the microphysical signatures of radar vertical profiles and lightning density. This study quantified the behavior of 5.3 million vertical profiles of the horizontal reflectivity (Z_H), differential reflectivity (Z_{DR}), specific differential phase (K_{DP}), and correlation coefficient (ρ_{HV}). The principal changes in the polarimetric variables occurred only for VHF source rate density greater than 14 VHF sources per km^2 in 4 min. These storms showed an enhanced positive K_{DP} in the mixed 1 layer (from 0 to −15°C) probably associated with supercooled liquid water signatures, whereas regions with negative Z_{DR} and K_{DP} and moderate Z_H in the mixed 2 layer (from −15 to −40°C) were possibly associated with the presence of conical graupel. The glaciated (above −40°C) and upper part of the mixed 2 layers showed a significant trend to negative K_{DP} with an increase in lightning density, in agreement with vertical alignment of ice particle by the cloud electric field. A conceptual model that presents the microphysical signatures in storms with and without lightning activity was constructed. The observations documented in this study provide an understanding of how the combinations of polarimetric variables could help to identify storms with different lightning density and vice versa.

1. Introduction

The next-generation of geostationary satellites that includes the Geostationary Operational Environmental Satellite–R (GOES-R) with Geostationary Lightning Mapper (GLM) sensor [*Goodman et al.*, 2013] and the Meteosat Third Generation (MTG) with Lightning Imager (LI) sensor [*Stuhlmann et al.*, 2005] will map total lightning activity continuously day and night with near-uniform spatial resolution of 8 km, frame rate of 2 ms, and a product latency of less than 20 s for GLM. The refinement of our current understanding about the processes relating cloud microphysical signatures and lightning density could be very useful for several applications, such as data assimilation [e.g., *Fierro et al.*, 2012, 2014; *Mansell*, 2014; *Qie et al.*, 2014], nowcasting [e.g., *Goodman et al.*, 1988; *Schultz et al.*, 2009, 2011, 2016], and rainfall estimation [e.g., *Soula*, 2009; *Wang et al.*, 2012; *Xu et al.*, 2013].

Storm microphysics plays a key role in the formation and lightning rate density. The noninductive (NI) charging of ice hydrometeors during rebounding collisions between ice particles (ice crystals and graupel) in an environment with supercooled water is the leading explanation for storm electrification [*Reynolds et al.*, 1957; *Takahashi*, 1978; *Saunders et al.*, 2006]. Several studies have suggested that in the NI charging process the charge centers built inside the cloud can produce an intense electric field (hundreds of kV/m) capable of exceeding the dielectric strength of air and driving the formation of electrical discharges [*Baker and Dash*, 1989; *Keith and Saunders*, 1990]. Laboratory studies have documented that the signal of charging is controlled by the relative growth rate (RGR) between two ice hydrometeors [*Saunders et al.*, 2006]. The NI-RGR mechanism is used to explain the tripolar charge structure within the updraft core regions [*Williams*, 1989; *Bruning et al.*, 2014]. Based on this picture several studies have suggested a well-established relationship between microphysical proprieties and lightning density [*Petersen and Rutledge*, 1998; *Wiens et al.*, 2005; *Schultz et al.*, 2015]. For example, *Petersen and Rutledge* [1998] described the increase in storm lightning density as the updraft strengthens and the ice particle volume in the mixed phase layer increases. Studies combining polarimetric radar and Lightning Mapping Array (LMA) have demonstrated a good correlation between the cloud microphysical properties and the regions with lightning production [*Krehbiel et al.*, 2000; *Wiens et al.*, 2005; *Bruning et al.*, 2007; *Lang and Rutledge*, 2008; *Payne et al.*, 2010]. *Wiens et al.* [2005] documented a

sudden increase in the number of very high frequency (VHF) sources and cloud-to-ground (CG) lightning density when an updraft stronger than 10 m s^{-1} exceeded 1500 km^3 and regions with graupel that exceeded 2000 km^3 in volume. More recently, *Schultz et al*. [2015] provided measurements of storm updraft properties and microphysics related to lightning jumps. The authors documented increases in graupel mass and updraft volumes greater than 10 m s^{-1} between the 10 and −40°C isotherms prior to the lightning jump. The occurrence of CG lightning has been documented close to regions with graupel and hail descending below the negative charge center [*Goodman et al*., 1989; *Carey and Rutledge*, 1996; *López and Aubagnac*, 1997; *Tessendorf et al*., 2007].

Consistent with this picture, polarimetric radar measurements have revealed key cloud properties related to lightning. Two polarimetric variables often used are the differential reflectivity (Z_{DR}) in the mixed phase layer (between 0 and −40°C) and the specific differential phase (K_{DP}) in the glaciated layer (between −40 and −65°C), which has been explored as a lightning indicator by several authors [i.e., *Caylor and Chandrasekar*, 1996; *Jameson et al*., 1996; *Carey and Rutledge*, 1996; *López and Aubagnac*, 1997; *Wiens et al*., 2005; *Lund et al*., 2009]. Z_{DR} is related to the ratio between the horizontal and vertical reflectivity (usually given in units of dB), while K_{DP} is related to the difference in phase shift between horizontal and vertical polarized pulses (usually given in units of degrees per kilometer) [*Straka et al*., 2000]. The work presented by *Lund et al*. [2009] showed two favorable layers for lightning initiation, including one layer between 3 and 6 km height with larger positive K_{DP} and positive Z_{DR} and a second layer between 7 and 10 km height with negative Z_{DR} and K_{DP}. In general, cloud regions just above a melting layer with deeper and positive Z_{DR} and K_{DP} are associated with supercooled raindrops and have been defined as Z_{DR}-columns, and their vertical extent is well correlated with the updraft intensity [*Picca et al*., 2010; *Kumjian et al*., 2012, 2014; *Homeyer and Kumjian*, 2015]. These regions are likely sources of graupel embryos, which may form via the freezing of drops in these columns [*Rutledge et al*., 1992; *Conway and Zrnić*, 1993; *Carey and Rutledge*, 1998]. Strong updrafts and the formation of graupel are favorable conditions for lightning production; therefore, the investigation of Z_{DR} columns could help to identify storms with and without lightning.

The glaciated phase region, defined here as the layer between −40 and −65°C (which in Brazil represents the cloud layer between 10.3 and 14.3 km mean sea level (msl)), presents specific polarimetric characteristics related to lightning. Several studies documented lightning onset in association with strongly negative Z_{DR} and K_{DP} in the glaciated layer [*Jameson et al*., 1996; *López and Aubagnac*, 1997]. *Caylor and Chandrasekar* [1996] found decreasing K_{DP} values at 12 km altitude prior to each lightning flash, and *Ventura et al*. [2013] reported simultaneous increase in lightning density with decrease in Z_{DR} and K_{DP} in this layer. The negative K_{DP} and Z_{DR} signatures are normally associated with vertically aligned ice particles by strong electric field [*Metcalf*, 1993, 1995; *Krehbiel et al*., 1996; *Caylor and Chandrasekar*, 1996; *Metcalf*, 1997; *Foster and Hallett*, 2002, 2008; *Carey et al*., 2009; *Ventura et al*., 2013; *Hubbert et al*., 2014]. *Weinheimer and Few* [1987] suggested that electrically active storms can induce instantaneous dipoles in pristine ice crystals that can align ice crystals. *Carey et al*. [2009] suggested that graupel falling with major axis vertically oriented can also be another reason for the negative K_{DP}. However, there is a consensus that negative K_{DP} signatures in the glaciated layer is at least partially associated with a strong electric field and physically connected to potential lightning.

Negative Z_{DR} has been also related to graupel particles. For example, *Dolan and Rutledge* [2009], using a T-matrix scattering model for several different hydrometeor types, suggested the presence of negative Z_{DR} associated with graupel particles. High-density graupel may have negative Z_{DR} values with relatively large reflectivity. Consistent with this picture, *Evaristo et al*. [2013] documented a linear decrease in Z_{DR} with the cone apex angle of graupel in conical format. However, it is unclear how much different are these signatures between storms with and without lightning activity. The majority of previous studies were based on case studies and describe the relationship between polarimetric radar signatures and lightning in a specific cloud height range. Studies quantifying statically how the storm polarimetric signatures, in each height range, vary as a function of the lightning density are absent. As graupel and ice crystals are key ingredients for storm electrification, the Z_H and K_{DP} signatures in higher-frequency radars, as the one employed in this study, could better distinguish differences between storms that produce lightning and those that do not.

The primary goal of this study is to evaluate, from the statistical point of view, the vertical distribution of the polarimetric variables as a function of lightning density, in this study expressed as VHF source rate density (number of sources per area per time). The combination of polarimetric signatures and VHF source rate

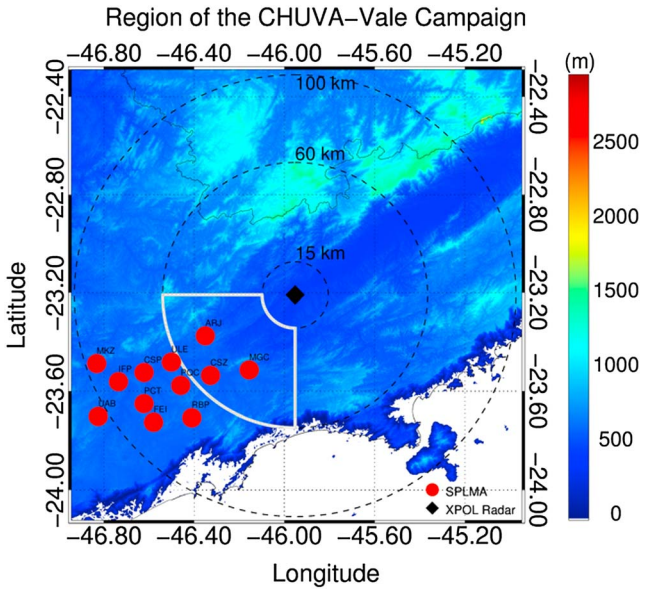

Figure 1. Region of CHUVA-Vale campaign, the XPOL radar (black diamond), and SPLMA network sensor (red filled circles) locations. The shaded region represents the elevation map (in meters), and the black dashed lines represent the distance rings (15, 60, and 100 km) from the radar. In this study we focused on the area highlighted in gray between 15 and 60 km far from the radar.

density helped to define the vertical microphysical properties of storms associated to different lightning patterns and the main differences between storms with and without lightning activity. Section 2 presents the general aspects of the CHUVA (Cloud Processes of the Main Precipitation Systems in Brazil: A Contribution to Cloud-Resolving Modeling and to the Global Precipitation Measurement (GPM))-Vale field campaign, radar data, preprocessing, LMA observations, and the methodology employed. Section 3 presents the relationship between polarimetric radar variables and lightning sources provided by a LMA network, and three cases studies employing lightning data detected by the Lightning Imaging Sensor (LIS), an example of data similar to that will be provided by GLM, to discuss the potential relationship between polarimetric radar data and lightning optical detections by satellites. Finally, section 4 presents the main conclusions.

2. CHUVA Experiment, Data, and Methodology

2.1. CHUVA-Vale Field Campaign

This study is based in the CHUVA-Vale field campaign held in São José dos Campos City, São Paulo State, Brazil, from 01 November 2011 to 31 March 2012. The CHUVA project was composed of six field campaigns throughout Brazil, with the objective of describing and understanding the cloud processes responsible for precipitation formation in the main precipitating regimes in Brazil. The complete description of the CHUVA project can be found in *Machado et al.* [2014]. The data are free access and are available in CHUVA project website (http://chuvaproject.cptec.inpe.br).

The region studied is located in a valley between the Mantiqueira and the Serra do Mar Mountains, approximately 100 km from the Atlantic Ocean. According to *Albrecht et al.* [2016], this region is prone to high thunderstorm activity (mean annual flash rate density above 30 flashes km^{-2} yr^{-1}), especially due to afternoon thunderstorms in the summer months (December to February). The main instruments employed in this work were a polarimetric X-band radar (Figure 1, circles of 15, 60 and 100 km range), LMA lightning network (Figure 1, red filled circles), and lightning events measured by the Tropical Rainfall Measuring Mission (TRMM) Lightning Imaging Sensor (LIS) sensor. Only the region highlighted in gray was selected for this study. This criterion was intended to ensure an area with good LMA detection efficiency (~100 km from the center of the network [see *Blakeslee et al.*, 2013; *Chmielewski and Bruning*, 2016]) and to delimit a region far enough from the radar to achieve the full vertical profile and close enough to avoid high-attenuation cases.

2.2. X-Band Radar and Data Preprocessing

The radar employed to measure the polarimetric signatures from the storm hydrometeors was a polarimetric X-band radar (9.34 GHz), hereafter referred to as XPOL, manufactured by Selex Gematronik, model Meteor 50DX. The volumetric scan strategy recorded four polarimetric variables: horizontal reflectivity (Z_H; dBZ), differential reflectivity (Z_{DR}; dB), specific differential phase (K_{DP}; °km^{-1}), and the correlation coefficient (ρ_{HV}) (see *Straka et al.* [2000] for a detailed description of these variables). The radar was installed at the Universidade do Vale do Paraíba at 650 m altitude above msl. The scan strategy comprised a volumetric scan, two range height

Table 1. Operating Parameters of the XPOL Radar During the CHUVA-Vale Campaign

Parameter	Characteristics
Operating frequency	9.375 GHz
Transmitter power	35 kW (magnetron, value per transmission channel)
Polarization	Simultaneous horizontal and vertical transmission
Pulse repetition frequency	1500/1200 Hz (stagger = 5/4, all elevations)
Antenna beamwidth	1.3°
Antenna diameter	1.8 m
Altitude of radar	650 m
Number of elevations	13 (1.0, 1.7, 2.6, 3.6, 4.8, 6.2, 7.8, 9.7, 11.9, 14.5, 17.5, 20.9, 25.0)°
Radial resolution (PPI)	150 m

indicator scans, and one vertical beam scan for the Z_{DR} offset correction. To complete all these tasks it was required approximately 6 min. The volumetric scan alone had duration of 4 min and consisted of 13 plan position indicators with elevations from 1.0° to 25.0°. Radar samples were resolved at 150 m in range and 1.0° in azimuth. Table 1 summarizes the principal characteristics of the XPOL radar and the volumetric scan strategy.

The radar data were preprocessed taking into account the following corrections: (i) the attenuation correction of the Z_H based in the algorithm proposed by *Testud et al*. [2000]. This algorithm constrains the reflectivity Z_H profile by the differential phase (PhiDP) to compensate the attenuation in Z_H when the radar pulse propagates through the rain medium. (ii) Correction of the differential attenuation in Z_{DR} using the linear PhiDP method. This method considers the total differential attenuation as linearly proportional to PhiDP (see *Bringi et al*. [2007] for a detailed description). The Z_{DR} average and median corrections were 0.16 and 0.32 dB, respectively. (iii) The Z_{DR} offset due to possible radar miscalibration was calculated by vertically pointing measurements during the radar scan sequence. Three distinct periods of offset corrections were defined during the CHUVA-Vale field campaign: the period before the replacement of the radome $\left(Z_{DR}^{off} = -0.27\ \text{dB}\right)$, the period after the replacement $\left(Z_{DR}^{off} = -0.33\ \text{dB}\right)$, and the period after radar maintenance $\left(Z_{DR}^{off} = -0.59\ \text{dB}\right)$. This correction was tested for hailstorms and strong rain events and the offset-corrected data sets improved the hydrometeor classification [*Sakuragi and Biscaro*, 2012]. The data used from the CHUVA project are level 1, and a detailed discussion of the CHUVA radar data preprocessing can be found in *Schneebeli et al*. [2012] and *Machado et al*. [2014].

2.3. São Paulo Lightning Mapping Array

The São Paulo Lightning Mapping Array (SPLMA) [*Blakeslee et al*., 2013] was deployed close to the metropolitan area of São Paulo and nearby cities during the CHUVA-Vale campaign (Figure 1, red filled circles). LMA systems locate electromagnetic emissions of lightning (i.e., lightning sources) originating from the breakdown processes of lightning propagation using the time of arrival of these sources at several stations every 80 ms [*Rison et al*., 1999; *Thomas et al*., 2001, 2004]. Each lightning flash emits tens to thousands of sources by mapping lightning propagation three dimensionally. The impulsive events are likely dominated by the negative leaders related to both IC and CG lightning. The advantage of the LMA network to infer charge centers is that a negative leader propagating into a positive-dominant charge region produces stronger VHF emission than a positive leader propagating into a negative-dominant charge region and so are detected more readily [*Rison et al*., 1999; *Williams*, 2006; *MacGorman et al*., 2008].

The SPLMA was composed of 12 stations operating on VHF TV channels 8 (180–186 MHz) and 10 (192–198 MHz) between November 2011 and March 2012 [*Bailey et al*., 2014]. With a network diameter of approximately 60 km, SPLMA provided accurate, three-dimensional lightning mapping to a range of 150 km, covering the area of radar surveillance selected for this study [*Blakeslee et al*., 2013]. To minimize the effect of noise, VHF sources detected by the SPLMA were limited to those with maximum reduced chi-square (χ^2) of 5 and detected by at least six stations. For the period of this study, the mean χ^2 and mean number of stations per solution were 1.3 and 7, respectively. Theoretical simulations performed for the SPLMA using the algorithm presented by *Koshak et al*. [2004] showed a location accuracy of approximately 1.0 km for the distance and height of the VHF sources, close to the radar center (W. Koshak, personal communication). Only the reprocessed data (level 1b), including information on the time, latitude, longitude, and height of the VHF sources, were used.

2.4. TRMM LIS Data

Lightning events measured by the Tropical Rainfall Measuring Mission (TRMM) Lightning Imaging Sensor (LIS) sensor were used for comparison with the polarimetric variables from XPOL radar. The LIS sensor detects optical emissions from lightning in the neutral oxygen line at the cloud top [*Goodman et al*., 2013; *Albrecht et al*., 2014b]. A charged coupled device takes measurements every 2 ms and compares to a background scene. Pixels that exceed a brightness threshold are identified as a lightning "event," which are clustered into "flashes" based on space and time proximity. Orbits of the TRMM satellite over the CHUVA-Vale region were selected, and the data used include information on the occurrence of every lightning event, as well as the latitude, longitude, and time of the event, and the viewtime of every scene.

2.5. Radar and Lightning Co-Located Data Set

To evaluate the polarimetric signatures as a function of the lightning density, we created a co-located data set between the radar vertical profiles and the VHF source information from the SPLMA. The first step was to reproject the polar coordinate volumetric radar scans into a Cartesian grid. This three-dimensional Cartesian box (hereafter called 3-D box) had grid cell spacing of 1 km × 1 km in the horizontal and 15 vertical levels of 1 km vertical resolution (hereafter called grid box). The grid box spacing (i.e., $1 \times 1 \times 1\ \mathrm{km}^3$) was defined consistently with the estimated localization error for the SPLMA (<1 km) and to reduce the effects of the low vertical resolution (~1 km) of the radar for higher elevations far from the radar. Each grid box was built by selecting the radar gate associated with the 95% percentile of the Z_H population in the $1\ \mathrm{km}^3$ grid box, and the associated Z_{DR}, K_{DP}, and ρ_{HV} of the radar gate were selected. The 95% percentile value was selected to choose the stronger reflectivity values in the $1\ \mathrm{km}^3$ grid box but still avoid the maximum values associated with incorrect or noisy measurements. Only vertical profiles associated with radar-reflective storms were used, i.e., profiles with some reflectivity value present.

After building the radar 3-D box, the SPLMA VHF sources were co-located in each $1\ \mathrm{km}^3$ radar grid box based on the nearest-neighbor method. Then, for each gridded radar vertical profile of polarimetric variables, the number of VHF sources occurring within the profile was integrated vertically (from 2 km to 15 km of height) and over the time interval of the radar volume scan (4 min) comprising one *VHF source rate density* for each vertical profile, in units of sources per kilometer square per 4 min ($\mathrm{src\ km^{-2}\ (4\ min)^{-1}}$). For simplicity, the VHF source rate density is also referred only as *lightning density*, hereinafter.

For practical purposes in cloud microphysics and cloud electrification, the air temperature profile was used as the vertical coordinate instead of heights in all figures. This association was based on the average temperature profile using 49 radiosondes launched close to the radar at 12 UTC. The mean melting level from the soundings was at 4.4 km msl.

To reduce the radar attenuation effects and to simultaneously ensure a region with good SPLMA detection efficiency, we used only the radar vertical profiles in the southwest quadrant of the radar coverage (region highlighted in gray) as shown in Figure 1. This region lies between 15 and 60 km from the radar center and is bounded by the radar azimuths of 180° and 270°. The minimum distance of 15 km eliminates the storm cases with limited tops due to the lower beam height close to the radar, and the maximum distance of 60 km reduces the attenuation effects. This methodology produced approximately 5.3 million radar vertical profiles of Z_H, Z_{DR}, K_{DP}, and ρ_{HV}, with every profile associated with a VHF source count.

3. Results and Discussion

3.1. Lightning Density

Figure 2 shows the frequency distribution of VHF lightning source rate density (i.e., lightning density) for all radar profiles. The number of radar vertical profiles decreases exponentially with the increase in the number of sources per square kilometer. The majority (~94%) of vertical profiles are associated with no sources, and only 305,108 radar profiles has more than one VHF source. Approximately two million sources were reported during the campaign; the average value of VHF source rate density was 8.6 $\mathrm{src\ km^{-2}\ (4\ min)^{-1}}$ with a standard deviation of 16.4 $\mathrm{src\ km^{-2}\ (4\ min)^{-1}}$, while the maximum value reported during the campaign was 430 $\mathrm{src\ km^{-2}\ (4\ min)^{-1}}$ (only one case). There were 94,823 cases (i.e., radar vertical profiles) with only

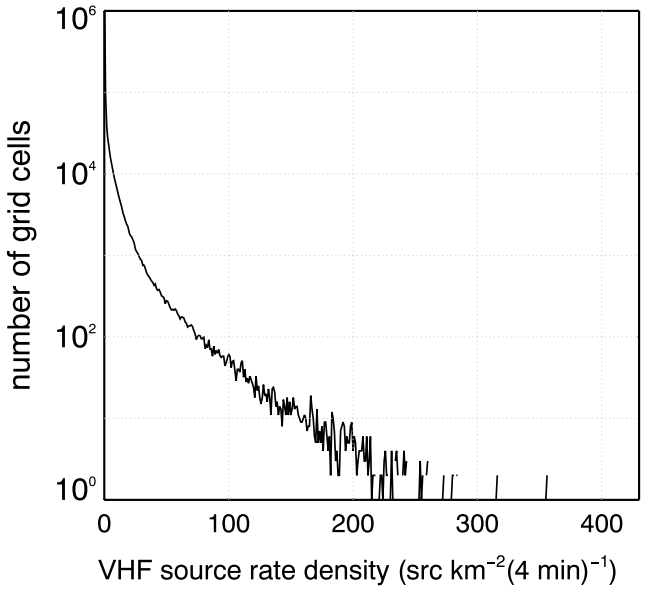

Figure 2. Frequency distribution of VHF source rate density (src km^{-2} (4 min)$^{-1}$) among all 3-D radar vertical profiles.

1 src km^{-2} (4 min)$^{-1}$, representing 31% of the population of the radar vertical profiles associated with at least one VHF source.

To evaluate the radar polarimetric characteristics as a function of the lightning density, the VHF source rate density was binned in classes of 5% percentiles. The percentiles correspond to profiles with more than one source per km^2 per 4 min. The cloud vertical structure was divided into four layers as follows: (i) warm (below 0°C, <4.4 km height), (ii) mixed 1 (from 0 to −15°C, 4.4 to 6.9 km height), (iii) mixed 2 (from −15 to −40°C, 6.9 to 10.3 km height), and (iv) glaciated (from −40 to −65°C, 10.3 to 14.3 km height) layers. Figure 3 shows the mean values of Z_H, Z_{DR}, K_{DP}, and ρ_{HV} as a function of the VHF source rate density percentiles (from 0 to 100%) for each of these cloud layers.

The percentiles up to 31% correspond to the bins of only one source, so they were grouped into only one category, named 0–30%. Three different behaviors are noted: (i) one class from the 0 to 65% percentiles (1 to 6 src km^{-2} (4 min)$^{-1}$), in which nearly no changes are observed in the polarimetric variables as the lightning density increases. Even in the warm phase layer (Figure 3a), very small changes are observed in the average properties; for instance, K_{DP} varies only from +0.5 to +0.8°km^{-1}. Z_{DR} decreases slightly from +0.65 to +0.60 dB in the mixed 1 layer between 0 and 55% percentiles. This modest change suggests that the average states of clouds with these lightning densities are very similar. The weaker variation in the mean values of the polarimetric variables is likely due to the fact that the mean was performed for a larger cloud layer, which probably smoothed the mean values. However, traditionally, singletons and flashes with few VHF sources could be attributable to noise effects (e.g., cell and television towers and transmission power lines). *Blakeslee et al*. [2013] studied the noise sources of the SPLMA and found that a TV tower on channel 9, in the middle of the SPLMA, produced noise sources that were detected by the network. They found that noise on the SPLMA was of very weak signal strength, concentrated within a short distance of the TV tower (90% of noise was within 1 km distance) and at altitudes lower than 5 km. This tower is about 25 km from the edge of our study area, and therefore, the effects of noise contamination in the data should be minimal. To verify this hypothesis, we have compared the signal strength of noise sources produced by the TV tower (using data during from nonthunderstorm days) and the signal strength of real sources used in our study. Sources from real lightning presented stronger signal strengths than noise-certain sources. The majority (considering the 10 and 90% percentiles) of noise sources presented signal strengths between −0.7 and +3.1 dBW and the sources from the lightning category with 1 to 6 src km^{-2} (4 min)$^{-1}$ presented between +3.1 and +14.5 dBW. Based on this analysis, we can claim that the sources of this lightning category are mostly related to real lightning flashes, and if any noise sources are present in the data, they constitute a very low percentage.

The second population (ii), from 7 to 13 src km^{-2} (4 min)$^{-1}$, corresponds to percentiles of 70 to 85%. This category shows weaker sensitivity as the lightning density increases. Z_H increases by 2 dBZ, Z_{DR} by 0.2 dB, and K_{DP} by 0.2°km^{-1} in the warm layer (Figure 3a). The third population (iii), more than 14 src km^{-2} (4 min)$^{-1}$, corresponds to grid cell populations with percentiles larger than 85%, and this category presented the most notable changes in the polarimetric variables with lightning density (Figures 3a–3d). K_{DP} increases from +1.2 to +2.2° km^{-1} as the lightning density increases in the warm layer, while in the glaciated layer K_{DP} decreases from +0.11 to −0.01°km^{-1}, suggesting a transition to conditions where ice particles are vertically oriented by a

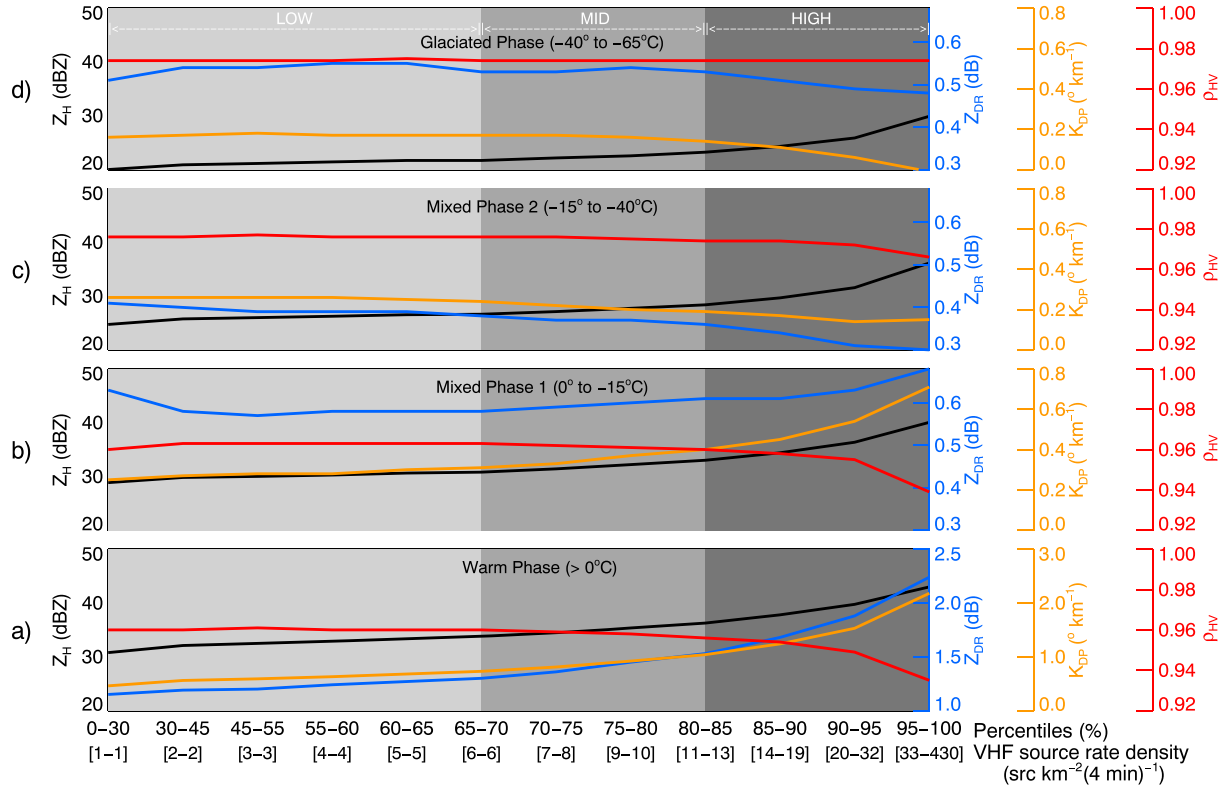

Figure 3. Mean values of Z_H (dBZ; black line), Z_{DR} (dB; blue line), K_{DP} (°km^{-1}; orange line), and ρ_{HV} (red line) as a function of VHF source rate density (src km^{-2} (4 min)$^{-1}$) percentiles (%) for (a) warm (below 0°C), (b) mixed 1 (from 0° to −15°C), (c) mixed 2 (from −15° to −40°C), and (d) glaciated (from −40° to −65°C) phase layers. The gray colors, from light gray to dark gray, show the lightning activity categories LOW, MID, and HIGH.

strong electric field. Z_{DR} presents similar behavior in comparison with K_{DP}, whereas the Z_H increases in all layers, with mean rate around 6 dBZ. These results suggest that a significant change in the polarimetric signatures as VHF source lightning rate density increases is only observed in the range of more than 14 src km^{-2} (4 min)$^{-1}$ and that larger change occur in the warm and mixed 1, followed by the mixed 2 and glaciated layers.

The aforementioned observations suggest the classification of the vertical profile population into four groups of lightning density as follows: (i) no sources, (ii) 1–6 src km^{-2} (4 min)$^{-1}$, (iii) 7–13 src km^{-2} (4 min)$^{-1}$, and (iv) 14–430 src km^{-2} (4 min)$^{-1}$. These groups of lightning activity categories are hereafter denoted, respectively, as NOVHF, LOW, MID, and HIGH. It is important to notice that the designations NOVHF, LOW, MID, and HIGH lightning activity categories are based on the specific population of profiles used in this study, which probably is different from other regions. Moreover, this definition is used in this study as a reference and only to classify the lightning density into categories.

Note that the number of sources here represents the sources recorded in a vertical column with 1 km^2 of area, which is different than traditional sources grouped into flashes. As the farthest point within our analysis region is 65 km from the center of the SPLMA, binning the VHF sources into flashes probably would exclude some real lightning events due to the decreased detection efficiency with increasing distance from the center of the network. Although the LOW VHF lightning activity category contains many fewer VHF sources (1–6 src km^{-2} (4 min)$^{-1}$), changes in the polarimetric signature are clearly observed (i.e., an increase in Z_H, Z_{DR}, and K_{DP} in the warm layer and mixed layer with the increase of lightning density). As we have used a large population of vertical radar profiles, if some noise exists for these small lightning density numbers, it did not affect the general statistics.

3.2. The Statistical Behavior of Polarimetric Variables

To evaluate the mean behavior of the polarimetric variables as a function of the predefined lightning activity categories (previous section), the mean radar vertical profile was computed (Figure 4). The colors in Figure 4

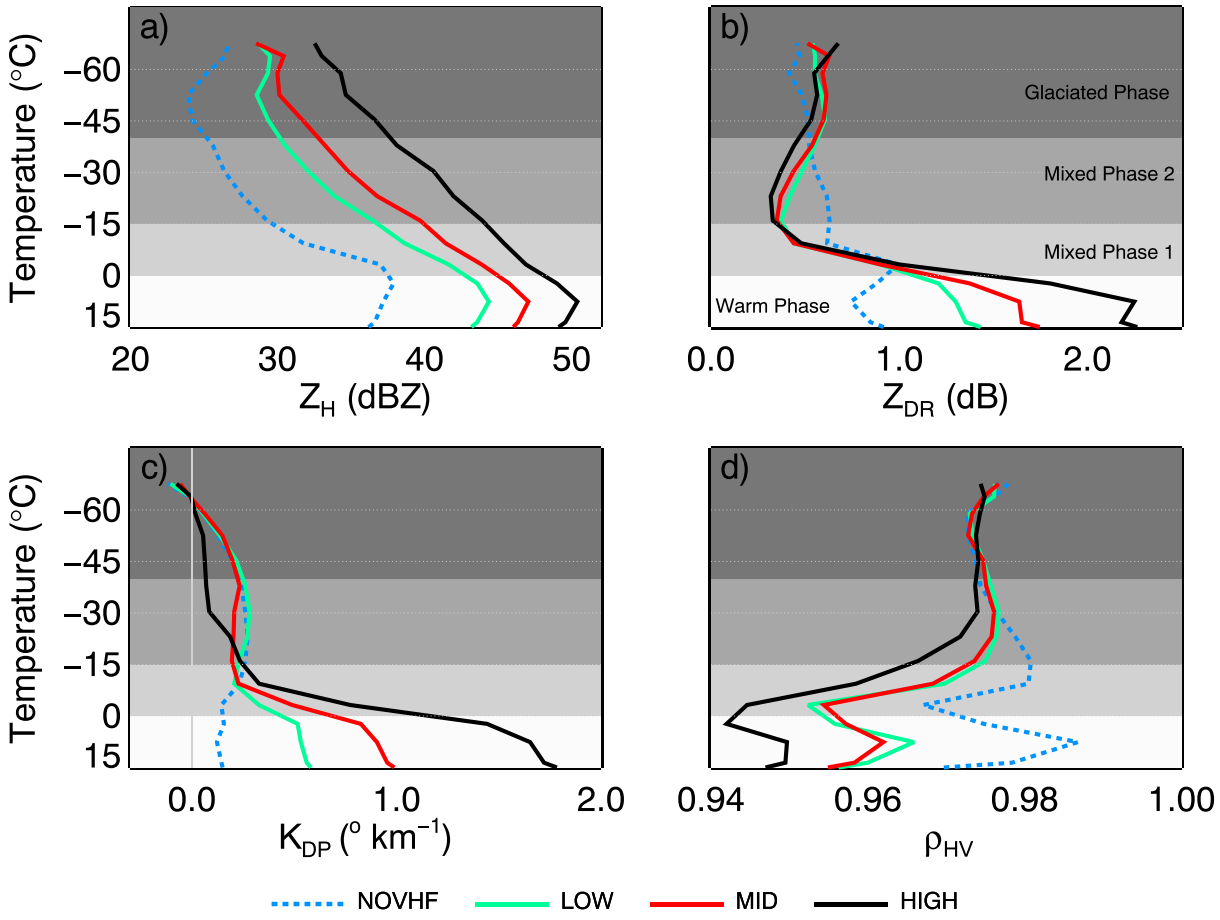

Figure 4. Mean profiles of (a) Z_H (dBZ), (b) Z_{DR} (dB), (c) K_{DP} (°km^{-1}), and (d) ρ_{HV} for the NOVHF (blue dashed line), LOW (green solid line), MID (red solid line), and HIGH (black solid line) categories of VHF source rate density. The gray vertical line in Figure 4c represents 0°km^{-1} for K_{DP}. The regions highlighted in gray colors indicate the layers of vertical profiles (warm, mixed 1, mixed 2, and glaciated phase layers).

represent the four predefined lightning activity categories: NOVHF (blue dashed line), LOW (green solid line), MID (red solid line), and HIGH (black solid line). The major differences between lightning activity categories (for all variables) occur in the warm phase layer (Figures 4a–4d, region in white color). In this layer, as the lightning density increases, Z_H, Z_{DR}, and K_{DP} dramatically increase, whereas ρ_{HV} decreases. For example, considering the 0°C level, K_{DP} (Figure 4c) increases by a factor of 7 from NOVHF (+0.2°km^{-1}) to HIGH (+1.4°km^{-1}) categories. These signatures suggest the existence of an intense precipitation process associated with strong concentration of larger oblate raindrops in the warm layer when the lighting density is the strongest. Moreover, resonance effects caused by these large raindrops could contribute to the higher Z_{DR} (Figure 4b) values and the low ρ_{HV} (Figure 4d) also observed in this layer [*Ryzhkov and Zrnic*, 2005]. However, if this effect is of the second order, the larger positive Z_{DR} (Figure 4b) and K_{DP} (Figure 4c) values and the lower ρ_{HV} (Figure 4d) for the HIGH class are probably associated with graupel from the mixed phase layer that is not completely melted and falling into the warm layer. These storms having stronger updrafts and larger graupel are formed in the balance-level region [*Lhermitte and Williams*, 1985], thereby intensifying the noninductive charging mechanism and lightning production. The aforementioned considerations are reinforced by the observed signatures in mixed 1 layer (from 0 to −15°C, region in light gray color). In the HIGH lightning category and above the 0°C level, Z_{DR} (Figure 4b) and K_{DP} (Figure 4c) values rapidly decrease to +0.3 dB and +0.2°km^{-1}, respectively, whereas ρ_{HV} (Figure 4d) increases up to 0.97, suggesting the freezing of large raindrops. Recently, similar observations were documented by *Mecikalski et al.* [2015], suggesting the existence of an intense freezing process leading to the formation of hail embryos, which quickly grow into graupel and hail through the riming process, contributing to intense electrification. However, decreased ρ_{HV} values close to the 0°C isotherm indicate the

existence of a mixture of hydrometeors possibly including supercooled raindrops, small hail, frozen drops, and graupel.

The striking characteristic in the mixed 2 layer (from −15 to −40°C, the region in medium gray color) is the decrease of K_{DP} (Figure 4c) with height reaching the lowest values (down to +0.1°km^{-1} close to the −40°C level) for the HIGH category, indicating that the number of frozen particles increased with height. In contrast, Z_{DR} (Figure 4b) in the mixed 2 layer is only slightly lower for the HIGH category throughout the layer but shows an increase with height. This behavior of Z_{DR} shows the increases in VHF source rate density as the updraft deepens, carrying supercooled liquid drops to higher levels [*Picca et al*., 2010; *Kumjian et al*., 2012, 2014; *Homeyer and Kumjian*, 2015]. Around −40°C level, from MID to HIGH lightning activity categories, K_{DP} decreases to +0.1°km^{-1} and Z_{DR} increases to +0.4 dB, indicating larger concentration of frozen particles. This change in the Z_{DR} and K_{DP} behavior observed between the upper part of the mixed 1 and throughout mixed 2 layer shows a clear transition, via freezing, to the formation of ice particles and graupel. For the glaciated layer (from −40 to −65°C, region in dark gray color), Z_H (Figure 4a) and K_{DP} (Figure 4c) show the greatest difference between the lightning categories. At the −45°C level, for instance, Z_H increases from 24 to 37 dBZ between the NOVHF and HIGH categories, whereas K_{DP} decreases from +0.2 to +0.05°km^{-1}. These observations suggest that a large concentration of ice particles with most of them aligned by strong electric field is a common signature in the glaciated layer. Interestingly, no difference is observed in K_{DP} between the categories NOVHF-LOW-MID in this layer (Figure 4c). These results show that a robust signature in K_{DP} as a function of VHF source rate density occurs only when there is a strong concentration of ice particles oriented by a strong electric field. As suggested by *Weinheimer and Few* [1987] and also shown by *Bailey and Hallett* [2009] habit diagram's, these ice particles probably are plates or columns, although columnar crystals between −40 and −70°C are much more likely to align than plate-like crystals.

Another interesting point observed in this figure is related to Z_{DR} (Figure 4b) in mixed 2 and the upper part of the mixed 1 layer. No differences in Z_{DR} are observed between the categories with lightning; suggesting ice particles with similar shape in this layer. In contrast, clouds associated with VHF sources have more negative Z_{DR} than clouds without lightning, a finding attributable to the formation of graupel. Similar observations were documented in lightning- and nonlightning-producing convective cells in thundersnow by *Kumjian and Deierling* [2015]. The authors documented that many of the flashes observed in thundersnow were associated with localized high-Z_H and low-Z_{DR} regions, suggesting regions with graupel production indicating that storms with lightning could have larger and more numerous graupel content than storms without lightning. Observations from ground-based total lightning combined with Doppler and polarimetric radar [*Deierling and Petersen*, 2008], numerical simulations with explicit microphysics [*Calhoun et al*., 2014], and satellite observations [*Mattos and Machado*, 2011; *Matthee and Mecikalski*, 2013] also support this idea, and it is suggested that storms with lightning include better graupel growth conditions due the existence of stronger updrafts, higher supercooled water content, and ice particle mass.

Table 2 shows the statistical distribution of the polarimetric variables as a function of lightning category for the different layers. This table presents the percentiles of 25%, 50%, and 75% for Z_H, Z_{DR}, K_{DP}, and ρ_{HV} for the warm, mixed 1, mixed 2, and glaciated phase layers for different lightning activity categories. In general, larger differences among lightning activity categories are found for the largest percentile (75% percentile), indicating regions with strong updrafts. Among all variables here analyzed, reflectivity showed the greatest difference among lightning activity categories for all layers. For example, in the warm layer, the median differs markedly from the NOVHF (16 dBZ) to HIGH (27 dBZ) categories. On the other hand, among the variables analyzed the K_{DP} shows the largest spread in distribution over the lightning activity categories in the warm layer. As the lightning density increases from the MID to HIGH category, the average K_{DP} increases 1.2°km^{-1} (i.e., change from +1.4 to +2.6°km^{-1}). This layer can be considered the final manifestation of all processes inside the cloud and represents the increase of the raindrop size, concentration, and nonhomogeneity as the storm becomes intense. Note that the negative K_{DP} (−0.1°km^{-1}) in the warm phase layer in the 25% percentile for the NOVHF category is probably related to nonuniform beam-filling effects [*Ryzhkov and Zrnic*, 2005; *Gosset*, 2004] near the melting layer.

In the mixed 1 layer, the variables Z_H and K_{DP} also showed high sensitivity as a function of lightning activity category. If the 75% percentile is considered, one can note an increase of 14 dBZ and 0.3°km^{-1} for Z_H and K_{DP},

Table 2. Percentiles of 25%, 50%, and 75% for Z_H, Z_{DR}, K_{DP}, and ρ_{HV} over the Warm, Mixed 1, Mixed 2, and Glaciated Phase Layers[a]

Storm Layer	Lightning Activity Categories	Z_H (dBZ)			Z_{DR} (dB)			K_{DP} (°km^{-1})			ρ_{HV}		
		P25	P50	P75	P25	P50	P75	P25	P50	P75	P25	P50	P75
Glaciated phase (from −40 to −65°C)	NOVHF	13	16	20	0.1	0.4	0.8	−0.1	0.1	0.4	0.96	0.98	1.00
	LOW	16	20	25	0.1	0.5	0.9	−0.1	0.2	0.5	0.97	0.98	0.99
	MID	17	22	28	0.1	0.4	0.9	−0.2	0.2	0.5	0.97	0.98	0.99
	HIGH	20	27	33	0.1	0.4	0.9	−0.3	0.1	0.4	0.97	0.98	0.99
Mixed phase 2 (from −15 to −40°C)	NOVHF	15	20	24	0.1	0.5	0.9	0.0	0.2	0.5	0.97	0.98	0.99
	LOW	21	25	30	0.1	0.3	0.7	0.0	0.2	0.5	0.97	0.98	0.99
	MID	22	27	33	0.0	0.3	0.7	−0.1	0.2	0.5	0.97	0.98	0.99
	HIGH	26	32	39	0.0	0.3	0.6	−0.2	0.2	0.5	0.97	0.98	0.99
Mixed phase 1 (from 0 to −15°C)	NOVHF	18	24	30	0.2	0.6	1.2	−0.1	0.2	0.4	0.94	0.97	0.99
	LOW	23	29	35	0.1	0.4	0.9	0.0	0.2	0.4	0.95	0.98	0.99
	MID	26	32	38	0.1	0.4	0.9	0.0	0.2	0.5	0.95	0.98	0.98
	HIGH	31	37	44	0.1	0.4	1.0	0.1	0.3	0.7	0.94	0.97	0.98
Warm phase (below 0°C)	NOVHF	18	25	32	0.2	0.6	1.2	−0.1	0.1	0.3	0.96	0.98	0.99
	LOW	24	31	39	0.5	1.0	1.7	0.0	0.2	0.7	0.95	0.97	0.98
	MID	28	35	43	0.6	1.3	2.2	0.1	0.5	1.4	0.95	0.97	0.98
	HIGH	33	41	48	1.0	1.9	2.7	0.4	1.2	2.6	0.93	0.96	0.98

[a]Percentiles are shown for the lightning activity categories with no source (NOVHF), low (LOW), middle (MID), and with the high (HIGH) VHF source rate densities.

respectively. This result demonstrates that the concentration and size of the supercooled raindrops in the mixed 1 layer increase as the lightning density increases. *Carey and Rutledge* [1998] suggested that this layer is the source of graupel embryos. Interestingly, the 25% and 75% percentiles of Z_H show no overlapping as one goes from NOVHF (18 and 30 dBZ) to HIGH (31 and 44 dBZ) lighting activity categories, suggesting the existence of a very different concentration of hydrometers. This result indicates an important role of Z_H in distinguishing between storms with and without lightning activity.

A striking characteristic in the mixed 2 layer is the observation of a near-zero and negative Z_{DR} and K_{DP} only for the MID and HIGH lightning density categories. The distribution of K_{DP} for HIGH lightning density shows negative values as low as $-0.2°km^{-1}$ for 25% percentile and Z_{DR} of 0.0 dB for the same percentile. These small values may be associated with conical graupel, as suggested by *Evaristo et al.* [2013]. We note that in the glaciated layer, the distribution of K_{DP} values is much more uniform in comparison with the other cloud layers discussed earlier, although a subtler decrease to exclusively negative values is observed in the 25% percentile for the HIGH lightning activity category, down to $-0.3°km^{-1}$. Similar to the mixed 1 layer, almost no overlapping occurs for Z_H percentiles between the NOVHF (13 and 20 dBZ) and HIGH (20 and 33 dBZ) lightning density categories. Because Z_H increases as a function of hydrometers size and concentration [*Battan*, 1973] and since the electrification process depends on both features of the ice particles that are colliding [*Keith and Saunders*, 1990], it is expected that a higher concentration of ice particles aligned vertically by a more intense electric field. However, some degrees of overlapping of polarimetric variables between the different lightning activity categories are observed, but the general differences between storms with and without lightning activity are very well captured.

Because the HIGH lightning category has the greatest changes in polarimetric characteristics with increasing rate density of sources (see Figure 3), we discretized this category into three subcategories. Figure 5 shows the evolution of the microphysics of clouds with the increased rate density of sources in this category, in which the polarimetric features are very sensitive. These subcategories have approximately 18,000 profiles in each category and are defined as follows: from 14 to 17 src km^{-2} (4 min)$^{-1}$ (the first 33% percentile) named HIGH1, from 18 to 29 src km^{-2} (4 min)$^{-1}$ (percentiles from 33 to 66%) named HIGH2, and larger than 30 src km^{-2} (4 min)$^{-1}$ (>66%) named HIGH3. Figure 5 shows the average profiles, similar to Figure 4, but for the three subcategories of HIGH lightning density.

The HIGH3 subcategory presents an average negative K_{DP} in the glaciated and in the upper part of the mixed 2 layers and reflectivity between 30 and 40 dBZ. This behavior occurs only for the most active lightning cases (i.e., larger than 30 src km^{-2} (4 min)$^{-1}$). In these subcategories, Z_{DR} varies only in the warm layer, showing

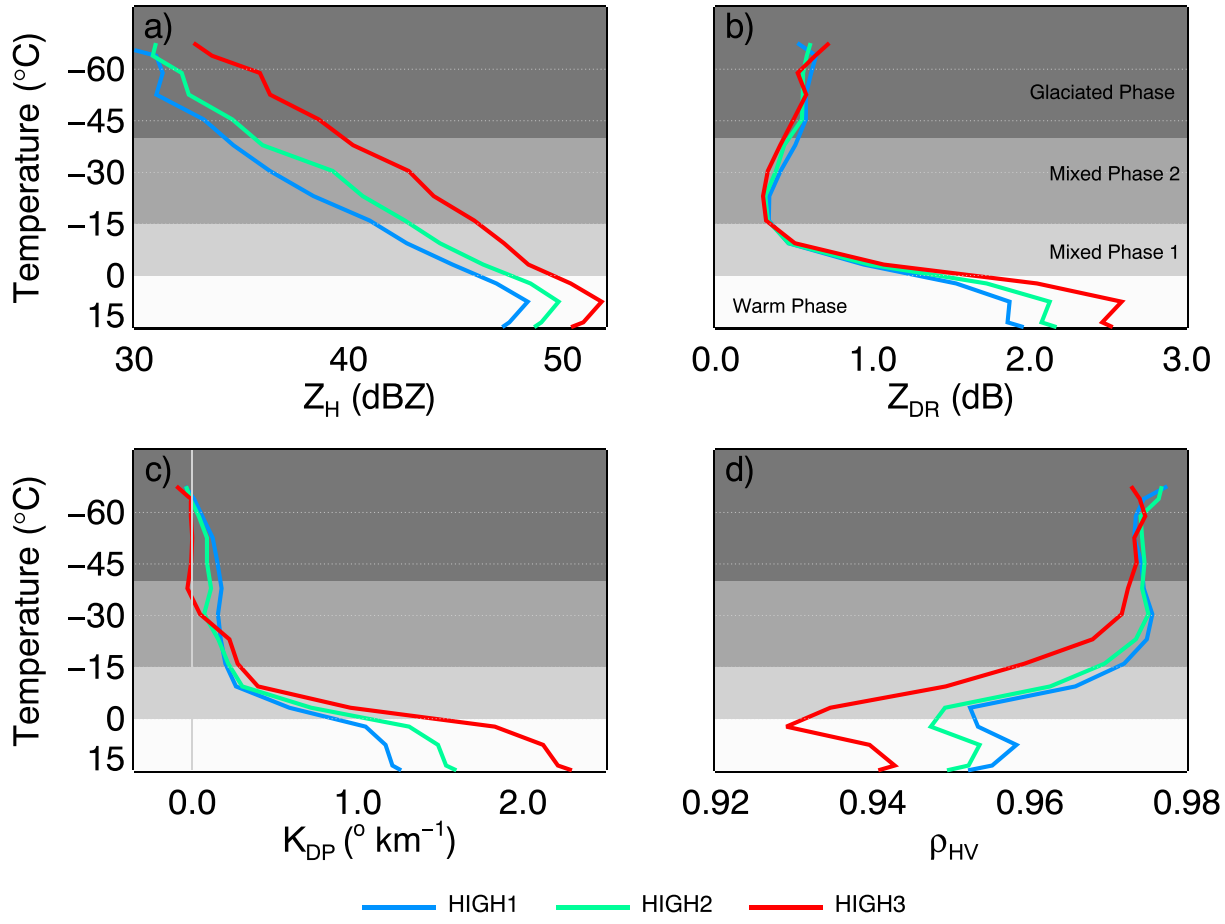

Figure 5. Mean profiles of (a) Z_H (dBZ), (b) Z_{DR} (dB), (c) K_{DP} (°km^{-1}), and (d) ρ_{HV} for the HIGH1 (blue solid line), HIGH2 (green solid line), and HIGH3 (red solid line) categories of lightning activity categories. The gray vertical line in Figure 5c represents 0°km^{-1} for K_{DP}. The regions highlighted in gray colors indicate the previously defined layers of vertical profiles (warm, mixed 1, mixed 2, and glaciated phase layers).

more oblate-large raindrops in the warm layer and nearly the same orientation in the other layers as the source rate density increases. Additionally, as ρ_{HV} in the mixed 1 and 2 and warm layers decrease the lightning density increases, showing the enhanced hydrometeor mixture in these layers. The Z_H in all layers and K_{DP} and Z_{DR} in the warm layer increase markedly as the source rate density increase. This characteristic can be useful for precipitation estimation in strongly convective storms when using lightning density information. This typical increase/decrease in values of polarimetric variables as the lightning density increases indicates that a large number of applications could be envisaged using future lightning sensors in geostationary satellites such as improve the precipitation estimation based on infrared channels, identify convective and stratiform regions of clouds, and provide assistance in the identification of the mean microphysical behavior of the cloud top.

The discussions pertaining to the Figures 4 and 5 showed individually the average behavior of each polarimetric variable as a function of the lightning density; however, the results do not ensure a synchronous behavior in all quantities. The joint interpretation of two or more polarimetric variables from the same grid box is much more effective and less prone to uncertainty and nonuniqueness than single-parameter analysis. This procedure often provides the best clues for inferring cloud processes and precipitation properties. As noted in previous analysis (i.e., Figures 3–5) Z_H, Z_{DR}, and K_{DP} were the variables that showed the most significant signatures in the predefined layers. Accordingly, these variables are considered for the joint interpretation of polarimetric variables. For this purpose, for each vertical profile, the data are binned as follows: from 0 to 60 dBZ in 6 dB increments for Z_H, from −2 to +6 dB in 0.8 dB increments for Z_{DR}, and from −2 to +6° km^{-1} in 0.8°km^{-1} increments for K_{DP}. This procedure was performed for each altitude range (i.e., warm,

mixed 1, mixed 2, and glaciated layers). The frequency distribution for every triple combination of Z_H-Z_{DR}-K_{DP} is normalized by the maximum frequency in each altitude range, such that the peak for each time is equal to one. To emphasize the most probable triple combinations only those combinations with higher relative frequency are plotted (>0.3%). Tests with different thresholds for the relative frequency were performed and indicated that the plot for triple combinations with frequency greater than 0.3% provided a good visualization of simultaneous behavior among Z_H-Z_{DR}-K_{DP} in all cloud layers. Figure 6 shows the simultaneous relationship among Z_H, Z_{DR}, and K_{DP} for NOVHF and HIGH lightning categories, and the colors represent the values for K_{DP}.

In the warm layer (Figure 6a) of the storm, the HIGH lightning category typically occurs in regions of higher Z_H values (up to 45 dB*Z*) while also containing uniquely higher positive Z_{DR} (up to +5.5 dB) and K_{DP} (up to +3.5° km^{-1}) than storms without lightning. The intermediate layers (i.e., mixed 1 and 2 layers; Figures 6b and 6c) show a transition from supercooled raindrops to frozen hydrometeors. Consistent with this behavior, the glaciated layer (Figure 6d) contains much lower Z_{DR} (down to −1.5 dB) and negative K_{DP} (down to $-2.0°km^{-1}$) values with moderate Z_H (<25 dB*Z*) values for HIGH lightning than for the category without lightning. Based on works presented by *Park et al*. [2009], *Dolan and Rutledge* [2009], and *Snyder et al*. [2010], these results suggest a higher concentration of vertically aligned ice particles by a strong electric field, here represented by the strongest lightning density, also evident in the mixed 2 layer. The strong support for a large concentration of supercooled raindrops in the mixed 1 layer for the higher lightning density is also observed. These regions are associated with graupel, most likely of conical shape. According to simulations from *Evaristo et al*. [2013], conical graupel is expected to have Z_H and Z_{DR} values ranging from 10 to 40 dB*Z* and from −1 to 1 dB, respectively. *Mattos* [2015] documented that for strongest storms the first lightning flashes were observed after positive Z_{DR} columns (associated with supercooled raindrops) evolved into much reduced Z_{DR} (and even negative values) in the mixed 1 layer before and during the time of the initial intracloud lightning, suggesting an evolution from supercooled raindrops to frozen particles, and the formation of graupel. Our results show that the melting process of graupel contributes to the formation of a larger concentration of large oblate raindrops observed in the warm layer.

The previous discussions showed a good relationship between the polarimetric variables signatures and the total sources integrated in the vertical profile. However, this relationship could be refined if one analyzed the relationship between the locations of VHF source in the vertical profile and the localization of polarimetric signatures. This strategy enables a determination of the storm regions with the maximum density of VHF sources and the associated polarimetric variables. For this purpose, each VHF source was associated with a specific temperature level (from height information) and was matched for a coincident value of Z_H, Z_{DR}, K_{DP}, and ρ_{HV}. Based on this procedure, we divided the temperature levels in 5°C bins (from 17 to −65°C) and the polarimetric variables in bins sizes of 2 dB*Z* (Z_H), 0.15 dB (Z_{DR}), $0.15°km^{-1}$ (K_{DP}), and 0.01 (ρ_{HV}). The number of VHF sources by temperature level and per polarimetric variable class was computed, and this value was normalized by the source number from all variable-temperature bins, which represent the relative frequency (%) of the sources. Figure 7 shows the relative frequency of the sources (color shaded region) and the total sources by height (red solid line).

In terms of the distribution of sources (color shaded region in Figure 7), the sources for the LOW category are spread over a large vertical region. As the electrical activity increases, the source concentration becomes more localized, and a maximum is located at higher altitudes between the temperatures −35 and −40°C for the HIGH category. This behavior can be associated with different stages of the storm electrification life cycle. Generally, stronger lightning density is documented prior to the maturation stage of the storm. Additionally, a secondary maximum in lightning sources is observed between −5 and −10°C, as evidenced for the HIGH category. These two maxima in number of sources are consistent with earlier studies [*Rison et al*., 1999; *Wiens et al*., 2005; *Lund et al*., 2009]. As discussed before, *Kumjian and Deierling* [2015] also documented snowstorms with stronger lightning density with maximum lightning density at higher altitudes. This suggests that although warm-season storms (as those studied here) have stronger updrafts than snowstorms, a similar process contributes to the cloud electrification and lightning production.

Typically, a negative leader propagating into a positive-dominant charge region produces stronger VHF emission than a positive leader propagating into a negative-dominant charge region [*Rison et al*., 1999; *Williams*, 2006]. Although only a detailed manual flash-by-flash analysis could allow the inference of specific charge

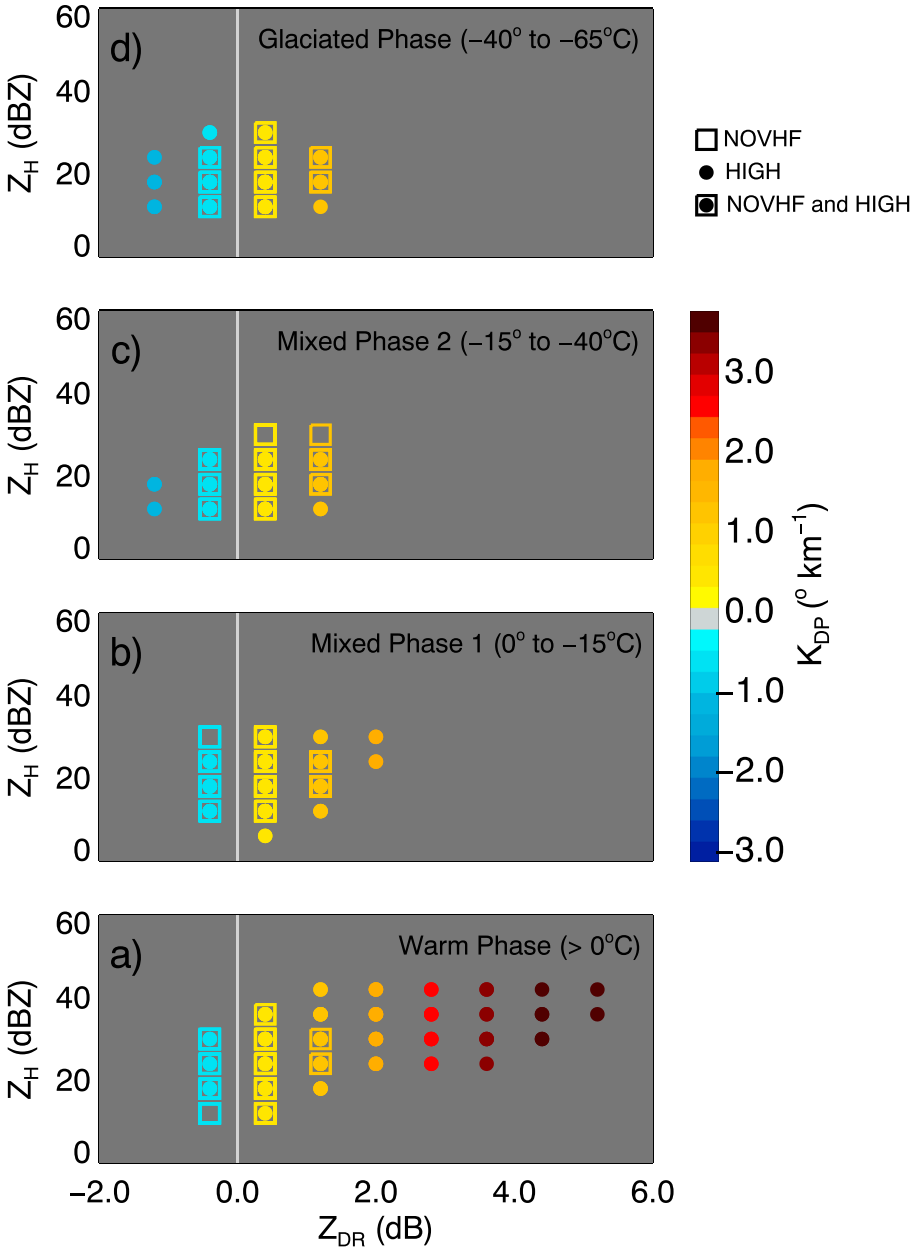

Figure 6. Three-dimensional histogram relating Z_H (ordinate), Z_{DR} (abscissa), and K_{DP} (color). Only triple bin combinations of Z_H-Z_{DR}-K_{DP} that presented highest frequency are plotted. The results are shown for NOVHF (open square) and HIGH (filled circle) lightning activity categories for the (a) warm, (b) mixed 1, (c) mixed 2, and (d) glaciated layers. Triple Z_H-Z_{DR}-K_{DP} combinations observed for both NOVHF and HIGH categories are represented by symbols with open square-filled circles.

regions (as those performed by *Wiens et al.* [2005], *Bruning et al.* [2007], *Lund et al.* [2009], and *Kumjian and Deierling* [2015]), the results of Figure 7 show a predominance of positive charge at higher altitudes (between −35 and −40°C).

With regard to the polarimetric variables, these regions with maximum lightning density have strong local relation with the storm microphysical properties and reinforce the previous analysis (i.e., Figures 4 and 5). The frequency line of 0.5% (white solid line) shows a relatively lower K_{DP} (down to −1°km^{-1}) for the HIGH category in comparison with the MID category (down to −0.6°km^{-1}) in the region between −35 and −40° C. In addition, the Z_H variable shows a bimodal distribution. Larger Z_H values close to the secondary source maximum (between −5 and −10°C) are observed for the HIGH category than for the MID category (50 dB*Z*

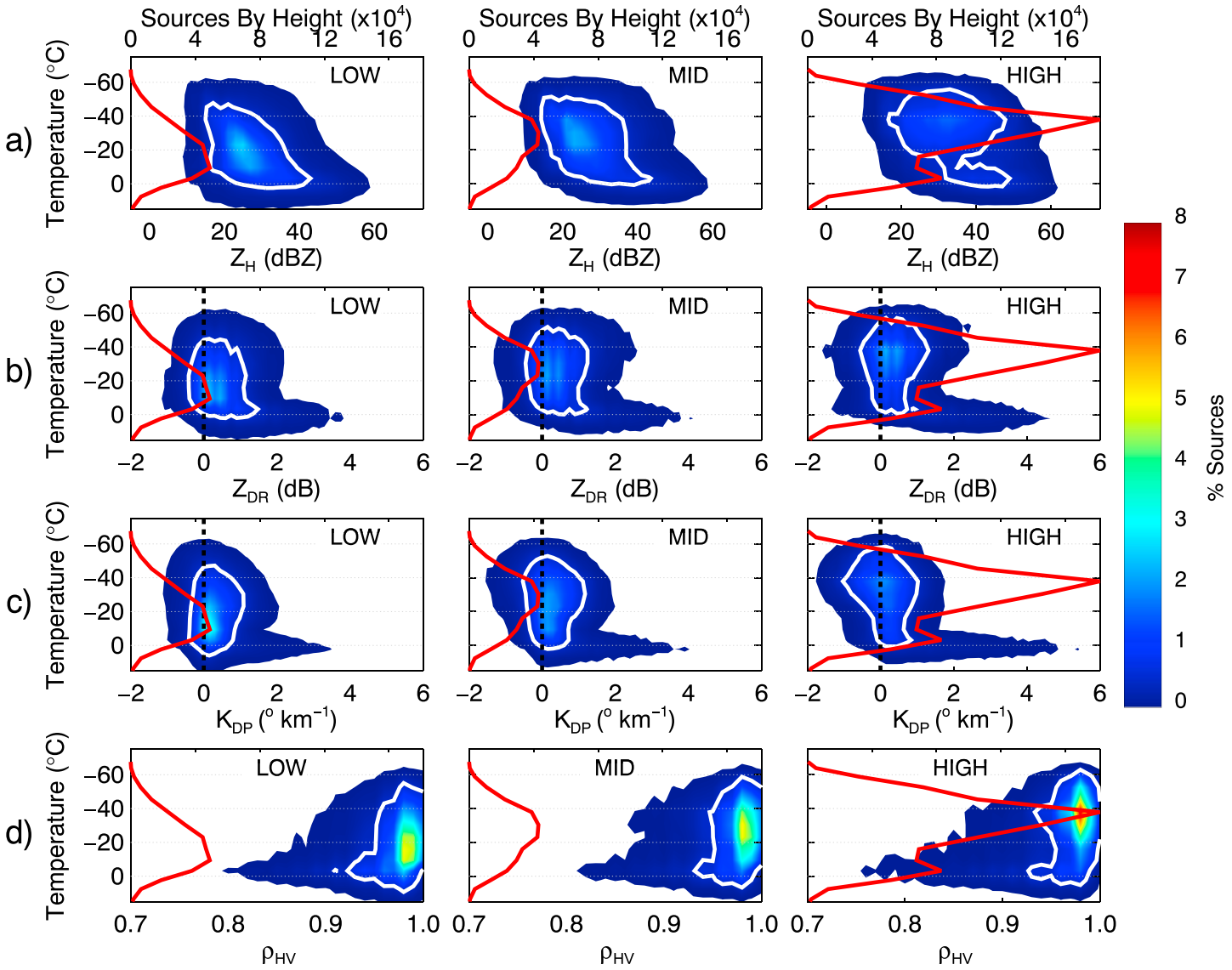

Figure 7. Distribution of normalized VHF sources (in %) for (a) Z_H (dBZ), (b) Z_{DR} (dB), (c) K_{DP} (°km^{-1}), and (d) ρ_{HV} for the LOW, MID, and HIGH lightning activity categories. The white solid line represents the 0.5% frequency contour. The total VHF source counts by temperature level (as a vertical profile) are superimposed as a red solid line.

versus 44 dBZ). The negative K_{DP} observed in the glaciated layer for the HIGH category corresponding to the regions with maximum sources reinforces the previous analyses and supports the electrification process discussed in the last sections. Additionally, these results suggest that the greatest differences among the lightning categories in terms of the polarimetric variables are in the regions that present the maximum density of VHF sources, that is, the region where vertically aligned ice by strong electric fields should occur.

This study is focused on a tropical region in a specific area and during a spring/summer season. Despite this meteorological focus, the results are very coherent with the cloud physics documented in several other works [*Caylor and Chandrasekar*, 1996; *Jameson et al.*, 1996; *Wiens et al.*, 2005; *Lund et al.*, 2009]. The applicability of these results should be investigated for several others environmental conditions (convective available potential energy and wind vertical shear) and for storms with different electrical structure (e.g., normal and inverted polarity storms).

3.3. TRMM LIS Lightning Events and XPOL Radar Vertical Profiles

Previous sections demonstrated a well-established relationship between the changes in hydrometeor vertical profiles and the lightning density. However, it is important to evaluate if this relationship described in this

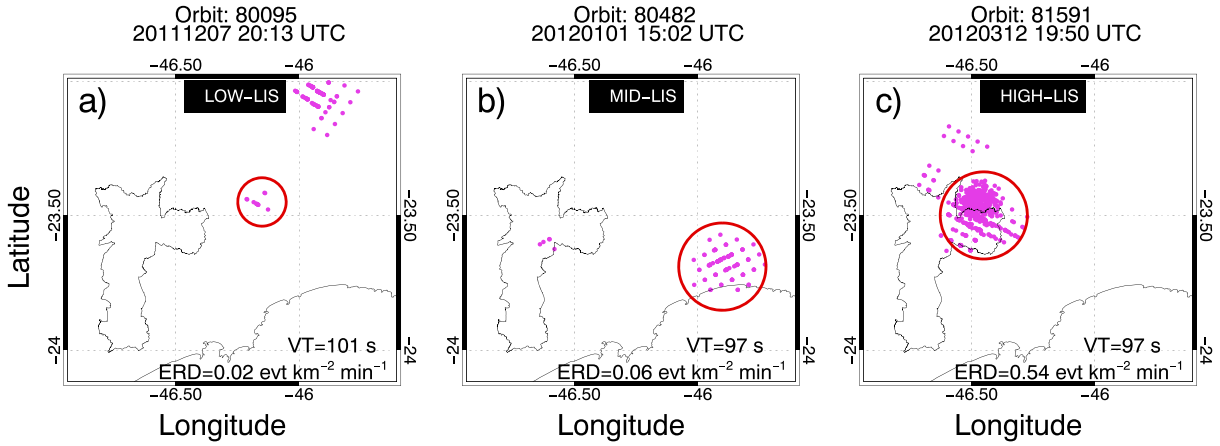

Figure 8. LIS lightning events for three storms with distinct lightning activity: (a) low (LOW-LIS; 0.02 evt km^{-2} min^{-1}), (b) middle (MID-LIS; 0.06 evt km^{-2} min^{-1}), and (c) high (HIGH-LIS; 0.54 evt km^{-2} min^{-1}). The TRMM LIS orbit and observation time are indicated in each plot.

study can also be observed for total lightning measured by satellites. This analysis could open an opportunity for future applications using total lightning measurements from GOES-R GLM and MTG LI to retrieve vertical microphysical properties in storms.

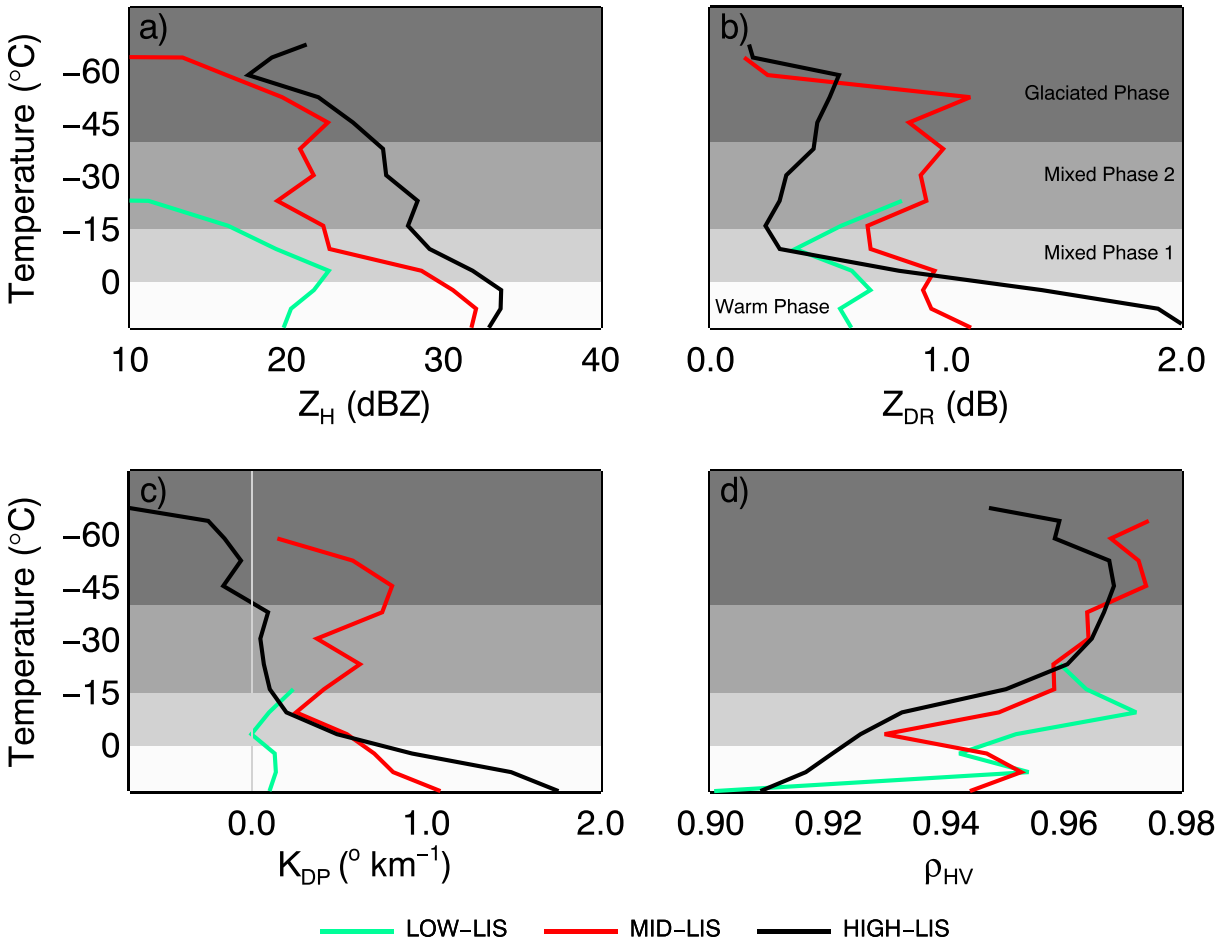

Figure 9. Mean profiles of polarimetric variables (a) Z_H (dBZ), (b) Z_{DR} (dB), (c) K_{DP} (°km^{-1}), and (d) ρ_{HV} for the LOW-LIS (green solid line), MID-LIS (red solid line), and HIGH-LIS (black solid line) lightning activity categories predefined in Figure 8. The gray vertical line in Figure 9c represents the 0°km^{-1} for K_{DP}. Regions highlighted in gray colors indicate the microphysical layers warm, mixed 1, mixed 2, and glaciated phase layers.

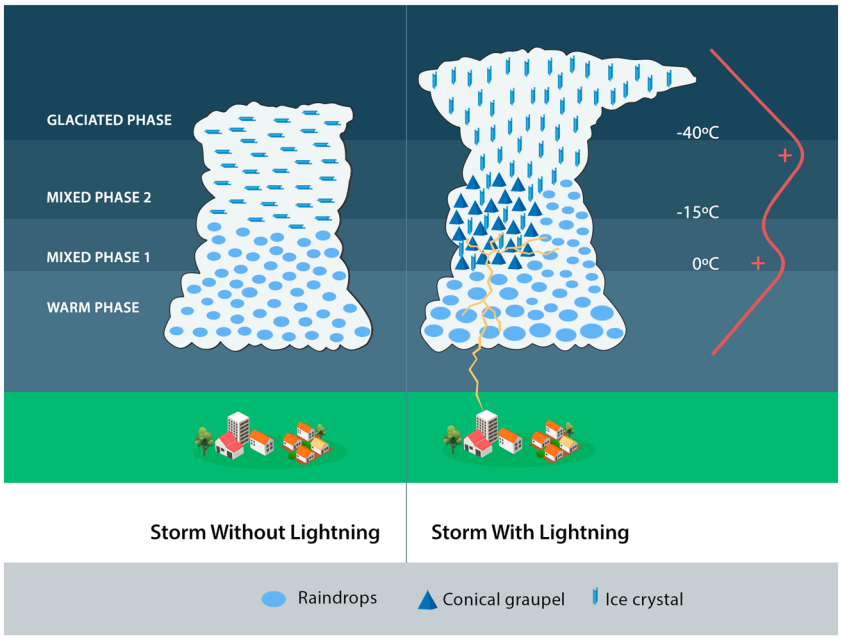

Figure 10. Schematic illustration of the main hydrometeor characteristics and VHF source count profile (red line) in storms with and without lightning activity.

For this proposal, three storms with different lightning events rate density on the radar area were selected: (i) one with relative low density (0.02 evt km^{-2} min^{-1}; 12 lightning events observed in 314 km^{-2} area during 101 s viewtime), (ii) one with relative middle density (0.06 evt km^{-2} min^{-1}; 106 lightning events observed in 1018 km^{-2} area during 97 s viewtime), and (iii) one with relative high density (0.54 evt km^{-2} min^{-1}; 884 lightning events observed in 1017 km^{-2} area during 97 s viewtime). LIS lightning events of these three cases are shown in Figure 8. The red circles represent the area of storms and define the region in which LIS lightning events were counted. LIS events were collocated with the 3-D radar data, and the mean vertical profile of each polarimetric variable was calculated using all profiles illuminated by the events, shown in Figure 9.

The most notable characteristic in Figure 9 is the increase in Z_H in all layers. Negative K_{DP} (Figure 9c) in the glaciated layer (down to $-0.7°km^{-1}$) is observed as the event density increases and lower Z_{DR} (Figure 9b) is observed for HIGH-LIS category in mixed 2 and glaciated layers. The profiles are very different for different event rate density, and the results are very similar to the one discussed in the former sessions for different VHF source rate densities. Although these analyses using LMA and LIS lightning showed some similarities in microphysical terms, it is important to clarify that LMA and LIS also involved different physics associated with the lightning measurement of each instrument. LMA systems detect electromagnetic emissions from lightning originating from the breakdown processes of lightning propagation [*Bruning and MacGorman*, 2013; *Albrecht et al*., 2014b], while optical emissions from the LIS are associated with the radiance from flashes at the cloud top [*Goodman et al*., 2013].

The measurements from LIS and GLM sensors are sensitive to scattering within the cloud medium. Therefore, lightning events documented in Figure 8 could suffer from effects of illumination by relatively close lightning. Part of this effect is associated with the radiative transfer problems and the LIS parallax error which are intrinsic effects of these measurements. Therefore, it is expected a better agreement between VHF sources and LIS lightning for VHF sources observed at higher heights (as discussed in *Albrecht et al*. [2014a]).

These results suggest that total lightning data from the GLM sensor can be useful for the retrieval of storm microphysical properties, such as the invigoration of the storm glaciated layer accompanied by an increase in the event source rate density (Figure 9). In addition, these results provide several meteorological applications such as improved understanding of cloud microphysical proprieties in regions with no radar coverage and improve or correct the precipitation estimates in regions with no radar or rain gauges using microphysical information or data assimilation of the microphysical proprieties in numerical models. The results

presented in this section are very promising; however, regional studies are necessary to evaluate how this relationship depends among the different types of storm, seasons, and regions.

4. Conclusions

This study evaluated the behavior of polarimetric signatures related to VHF source rate density in different layers of cumulonimbus clouds. For the first time, a large data set of vertical profiles of polarimetric radar observations combined with tridimensional VHF sources was employed to represent a statistical pattern of storm hydrometeors associated with lightning density.

The most notable changes in storm polarimetric properties occurred for lightning density greater than 14 sources per km^2 in 4 min, and the cloud polarimetric properties change markedly with the VHF source rate density in this range. K_{DP} increases by a factor of 2 in the warm layer and decreases by 10 times in the glaciated layer when the lightning density changes from 14 to 430 src km^{-2} $(4\,min)^{-1}$. These changes are most clearly manifest in the warm layer and indicate the formation of larger raindrops probably associated with the melting of larger graupel in the mixed layer. However, a typical polarimetric behavior is documented for each of the categories of VHF source rate density defined in this study. The warm layer shows increases in Z_H, Z_{DR}, and K_{DP} as the rate density of source increases, suggesting a stronger precipitation process for the formation of larger flattened raindrops. The mixed 1 layer shows a typical signature of supercooled liquid water as the VHF source rate density increases. This behavior of moderate reflectivity is associated with larger and strong updraft regions, where supercooled liquid water is carried to higher levels in the mixed 1 layer. An increase in the height of positive K_{DP} is documented as the VHF source rate density increases. Our results are consistent with those presented by *Mattos* [2015] and suggest that the regions of negative Z_{DR} and K_{DP} with moderate Z_H are associated with the presence of conical graupel. The mixed 2 layer showed a well-defined increase in negative values of Z_{DR} and K_{DP} associated with weak Z_H as the VHF source rate density moves to highest values of VHF source rate density. In the glaciated layer, a large amount of vertically aligned ice crystals in a strong electric field is documented mainly for a density of sources larger than 30 per km^2 in 4 min. The glaciated and upper part of the mixed 2 layers show a significant trend toward negative K_{DP} with an increase in the lightning density, in agreement with the theory of ice crystal alignment by the cloud electric field. Needles and columns are the most probable radar target for these signatures. The values presented in Table 2 can be used as guidance for VHF source rate density and to support future nowcasting algorithms using polarimetric radar operating at X-band frequency. The combined use of VHF sources and polarimetric signatures might be helpful in locating storms that are highly charged but have not yet produced lightning. The LIS lightning events and polarimetric measurements showed very similar behavior compared with those observed for VHF sources, i.e., negative values of K_{DP} in the glaciated layer and lower Z_{DR} values at higher layers in stronger storms. Based on these results, a conceptual model is presented in Figure 10 for storms with and without lightning activity.

These results open a perspective to the use the total lightning from GLM sensor as auxiliary information to try retrievals of the storm microphysical properties. However, this relationship needs to be evaluated for other regions, seasons, and different storms. Future work should explore the above observations on a storm-by-storm basis, considering the storm life cycle. This paper has shown that the intrusion of supercooled raindrops in the mixed 1 layer is well correlated with the VHF source rate density and that a conspicuous negative K_{DP} in upper levels is observed primarily in situations with the highest lightning density. In this way, the evolution of the cloud transitioning from storm to thunderstorm can aid the understanding of lightning formation from the first radar echo to the time of the first intracloud and cloud-to-ground lightning.

Acknowledgments

We would like to thank Fundação de Amparo à Pesquisa do Estado de São Paulo for the financial support of CHUVA project (grant 2009/15235-8) and the PhD scholarship for the first author of this paper (grant 2011/18217-0). We acknowledge the GOES-R Program, which provided the SPLMA network data from the CHUVA-Vale campaign, and Jeffrey Bailey (University of Alabama in Huntsville) and Richard J. Blakeslee (NASA MSFC) for providing and reprocessing the LMA data and for many discussions. In addition, we would like to thank Thiago S. Biscaro (INPE CPTEC) for the radar data processing. The data used in this work are freely accessible and are available at the CHUVA project website (http://chuva-project.cptec.inpe.br). Finally, we would like to thank Michael J. Peterson (ESSIC-UMD) and the two other anonymous reviewers for their helpful comments.

References

Albrecht, R. I., C. A. Morales, C. M. N. Iwabe, M. F. Saba, and H. Höller (2014a), Using lightning mapping array to evaluate the lightning detection signatures at different technologies, paper presented at XV International Conference on Atmospheric Electricity, Int. Comm. on Atmos. Electr., Norman, Okla.

Albrecht, R. I., D. J. Cecil, and S. J. Goodman (2014b), Lightning, in *Encyclopedia of Remote Sensing SE-86*, edited by E. G. Njoku, pp. 339–344, Springer, New York.

Albrecht, R. I., S. J. Goodman, D. E. Buechler, R. J. Blakeslee, and H. J. Christian (2016), Where are the lightning hotspots on Earth?, *Bull. Am. Meteorol. Soc.*, doi:10.1175/BAMS-D-14-00193.1.

Bailey, J. C., R. J. Blakeslee, L. D. Carey, S. J. Goodman, S. D. Rudlosky, R. Albrecht, C. A. Morales, E. M. Anselmo, J. R. Neves, and D. E. Buechler (2014), São Paulo Lightning Mapping Array (SP-LMA): Network assessment and analyses for intercomparison studies and GOES-R proxy

activities, paper presented at XV International Conference on Atmospheric Electricity, International Commission on Atmospheric Electricity, Norman, OK, USA.
Bailey, M. P., and J. Hallett (2009), A comprehensive habit diagram for atmospheric ice crystals: Confirmation from the laboratory, AIRS II, and other field studies, *J. Atmos. Sci.*, *66*, 2888–2899, doi:10.1175/2009JAS2883.1.
Baker, M. B., and J. G. Dash (1989), Charge transfer in thunderstorms and the surface melting of ice, *J. Cryst. Growth*, *97*, 770–776, doi:10.1016/0022-0248(89)90581-2.
Battan, L. J. (1973), *Radar Observation of the Atmosphere*, Univ. of Chicago Press, Chicago, Ill.
Blakeslee, R. J., J. C. Bailey, L. D. Carey, S. J. Goodman, S. D. Rudlosky, R. Albrecht, C. A. Morales, E. M. Anselmo, and J. R. Neves (2013), São Paulo Lightning Mapping Array (SP-LMA): Network assessment and analyses for intercomparison studies and GOES-R proxy activities, paper presented at CHUVA International Workshop, São Paulo, SP, Brazil.
Bringi, V. N., M. Thurai, and R. Hannesen (2007), Correcting the measured Z_{DR} for differential attenuation due to rain, in *Dual-Polarization Weather Radar Handbook*, Selex-SI Gematronik, Neuss, Germany.
Bruning, E. C., and D. R. MacGorman (2013), Theory and observations of controls on lightning flash size spectra, *J. Atmos. Sci.*, *70*(12), 4012–4029, doi:10.1175/JAS-D-12-0289.1.
Bruning, E. C., W. D. Rust, T. J. Schuur, D. R. MacGorman, P. R. Krehbiel, and W. Rison (2007), Electrical and polarimetric radar observations of a multicell storm in TELEX, *Mon. Weather Rev.*, *135*, 2525–2544, doi:10.1175/MWR3421.1.
Bruning, E. C., S. A. Weiss, and K. M. Calhoun (2014), Continuous variability in thunderstorm primary electrification and an evaluation of inverted-polarity terminology, *Atmos. Res.*, *135-136*, 274–284, doi:10.1016/j.atmosres.2012.10.009.
Calhoun, K. M., E. R. Mansell, D. R. MacGorman, and D. C. Dowell (2014), Numerical simulations of lightning and storm charge of the 29–30 May 2004 Geary, Oklahoma, supercell thunderstorm using EnKF mobile radar data assimilation, *Mon. Weather Rev.*, *142*, 3977–3997, doi:10.1175/MWR-D-13-00403.1.
Carey, L. D., and S. A. Rutledge (1996), A multiparameter radar case study of the microphysical and kinematic evolution of a lightning producing storm, *Meteorol. Atmos. Phys.*, *59*, 33–64, doi:10.1007/BF01032000.
Carey, L. D., and S. A. Rutledge (1998), Electrical and multiparameter radar observations of a severe hailstorm, *J. Geophys. Res.*, *103*, 13,979–14,000, doi:10.1029/97JD02626.
Carey, L. D., W. A. Petersen, and W. K. Deierling (2009), Radar differential phase signatures of ice orientation for the prediction of lightning initiation and cessation, paper presented at 34th Conference on Radar Meteorology, Am. Meteorol. Soc., Williamsburg, Va.
Caylor, I. F., and V. Chandrasekar (1996), Time-varying ice crystal orientation in thunderstorms observed with multiparameter radar, *IEEE Trans. Geosci. Electron.*, *34*, 847–858, doi:10.1109/36.508402.
Chmielewski, V. C., and E. C. Bruning (2016), Lightning Mapping Array flash detection performance with variable receiver thresholds, *J. Geophys. Res. Atmos.*, *121*, 8600–8614, doi:10.1002/2016JD025159.
Conway, J. W., and D. S. Zrnić (1993), A study of embryo production and hail growth using dual-Doppler and multiparameter radars, *Mon. Weather Rev.*, *121*, 2512–2528, doi:10.1175/1520-0493(1993)121<2511:ASOEPA>2.0.CO;2.
Deierling, W., and W. A. Petersen (2008), Total lightning activity as an indicator of updraft characteristics, *J. Geophys. Res.*, *113*, D16210, doi:10.1029/2007JD009598.
Dolan, B., and S. A. Rutledge (2009), A theory-based hydrometeor identification algorithm for X-band polarimetric radars, *J. Atmos. Oceanic Technol.*, *26*, 2071–2088, doi:10.1175/2009JTECHA1208.1.
Evaristo, R., T. M. Bals-Elsholz, E. R. Williams, D. J. Smalley, M. F. Donovan, and A. Fenn (2013), Relationship of graupel shape to differential reflectivity: Theory and observations, paper presented at 93rd American Meteorological Society Annual Meeting, Am. Meteorol. Soc., Austin, Tex.
Fierro, A. O., E. R. Mansell, C. L. Ziegler, and D. R. MacGorman (2012), Application of a lightning data assimilation technique in the WRF-ARW model at cloud-resolving scales for the tornado outbreak of 24 May 2011, *Mon. Weather Rev.*, *140*, 2609-–2627, doi:10.1175/MWR-D-11-00299.1.
Fierro, A. O., J. Gao, C. L. Ziegler, E. R. Mansell, D. R. Macgorman, and S. R. Dembek (2014), Evaluation of a cloud-scale lightning data assimilation technique and a 3DVAR method for the analysis and short-term forecast of the 29 June 2012 Derecho event, *Mon. Weather Rev.*, *142*, 183–200, doi:10.1175/MWR-D-13-00142.1.
Foster, T. C., and J. Hallett (2002), The alignment of ice crystals in changing electric fields, *Atmos. Res.*, *62*, 149–169, doi:10.1016/S0169-8095(02)00008-X.
Foster, T. C., and J. Hallett (2008), Enhanced alignment of plate ice crystals in a non-uniform electric field, *Atmos. Res.*, *90*, 41–53, doi:10.1016/j.atmosres.2008.02.017.
Goodman, S. J., D. E. Buechler, P. D. Wright, and W. D. Rust (1988), Lightning and precipitation history of a microburst-producing storm, *Geophys. Res. Lett.*, *15*, 1185-–1188, doi:10.1029/GL015i011p01185.
Goodman, S. J., D. E. Buechler, P. D. Wright, W. D. Rust, and K. E. Nielsen (1989), Polarization radar and electrical observations of microburst producing storms during COHMEX, paper presented at 24th Conference on Radar Meteorology, Am. Meteorol. Soc., Tallahassee, Fla.
Goodman, S. J., et al. (2013), The GOES-R Geostationary Lightning Mapper (GLM), *Atmos. Res.*, *125-126*, 34–49, doi:10.1016/j.atmosres.2013.01.006.
Gosset, M. (2004), Effect of nonuniform beam filling on the propagation of radar signals at X-band frequencies. Part II: Examination of differential phase shift, *J. Atmos. Oceanic Technol.*, *21*, 358–367, doi:10.1175/1520-0426(2004)021<0358:EONBFO>2.0.CO;2.
Homeyer, C. R., and M. R. Kumjian (2015), Microphysical characteristics of overshooting convection from polarimetric radar observations, *J. Atmos. Sci.*, *72*, 870–891, doi:10.1175/JAS-D-13-0388.1.
Hubbert, J. C., S. M. Ellis, W.-Y. Chang, S. Rutledge, and M. Dixon (2014), Modeling and interpretation of S-band ice crystal depolarization signatures from data obtained by simultaneously transmitting horizontally and vertically polarized fields, *J. Appl. Meteorol. Climatol.*, *53*, 1659–1677, doi:10.1175/JAMC-D-13-0158.1.
Jameson, A. R., M. J. Murphy, and E. P. Krider (1996), Multiple-parameter radar observations of isolated Florida thunderstorms during the onset of electrification, *J. Appl. Meteorol.*, *35*, 343–354, doi:10.1175/1520-0450(1996)035<0343:MPROOI>2.0.CO;2.
Keith, W. D., and C. P. R. Saunders (1990), Further laboratory studies of the charging of graupel during ice crystal interactions, *Atmos. Res.*, *25*, 445–464, doi:10.1016/0169-8095(90)90028-B.
Koshak, W. J., et al. (2004), North Alabama Lightning Mapping Array (LMA): VHF source retrieval algorithm and error analyses, *J. Atmos. Oceanic Technol.*, *21*, 543-–558, doi:10.1175/1520-0426(2004)021<0543:NALMAL>2.0.CO;2.
Krehbiel, P., T. Chen, S. McCrary, W. Rison, G. Gray, and M. Brook (1996), The use of dual channel circular-polarization radar observations for remotely sensing storm electrification, *Meteorol. Atmos. Phys.*, *59*, 65–82, doi:10.1007/BF01032001.

Krehbiel, P. R., R. J. Thomas, W. Rison, T. Hamlin, J. Hamlin, and M. Davis (2000), GPS-based mapping system reveals lightning inside storms, *Eos Trans. AGU*, *81*, 21–25, doi:10.1029/00EO00014.

Kumjian, M. R., and W. Deierling (2015), Analysis of thundersnow storms over northern Colorado, *Weather Forecast.*, *30*, 1469–1490, doi:10.1175/WAF-D-15-0007.1.

Kumjian, M. R., S. M. Ganson, and A. V. Ryzhkov (2012), Freezing of raindrops in deep convective updrafts: A microphysical and polarimetric model, *J. Atmos. Sci.*, *69*, 3471–3490, doi:10.1175/JAS-D-12-067.1.

Kumjian, M. R., A. P. Khain, N. Benmoshe, E. Ilotoviz, A. V. Ryzhkov, and V. T. J. Phillips (2014), The anatomy and physics of Z_{DR} columns: Investigating a polarimetric radar signature with a spectral bin microphysical model, *J. Appl. Meteorol. Climatol.*, *53*, 1820–1843, doi:10.1175/JAMC-D-13-0354.1.

Lang, T. J., and S. A. Rutledge (2008), Kinematic, microphysical, and electrical aspects of an asymmetric bow-echo mesoscale convective system observed during STEPS 2000, *J. Geophys. Res.*, *113*, D08213, doi:10.1029/2006JD007709.

Lhermitte, R., and E. Williams (1985), Thunderstorm electrification: A case study, *J. Geophys. Res.*, *90*, 6071–6078, doi:10.1029/JD090iD04p06071.

López, R. E., and J.-P. Aubagnac (1997), The lightning activity of a hailstorm as a function of changes in its microphysical characteristics inferred from polarimetric radar observations, *J. Geophys. Res.*, *102*, 16,799–16,813, doi:10.1029/97JD00645.

Lund, N. R., D. R. MacGorman, T. J. Schuur, M. I. Biggerstaff, and W. D. Rust (2009), Relationships between lightning location and polarimetric radar signatures in a small mesoscale convective system, *Mon. Weather Rev.*, *137*, 4151–4170, doi:10.1175/2009MWR2860.1.

MacGorman, D. R., et al. (2008), TELEX: The Thunderstorm Electrification and Lightning Experiment, *Bull. Am. Meteorol. Soc.*, *89*, 997––1013, doi:10.1175/2007BAMS2352.1.

Machado, L. A. T., et al. (2014), The CHUVA project—How does convection vary across the Brazil?, *Bull. Am. Meteorol. Soc.*, doi:10.1175/BAMS-D-13-00084.1.

Mansell, E. R. (2014), Storm-scale ensemble Kalman filter assimilation of total lightning flash-extent data, *Mon. Weather Rev.*, *142*, 3683–3695, doi:10.1175/MWR-D-14-00061.1.

Matthee, R., and J. R. Mecikalski (2013), Geostationary infrared methods for detecting lightning-producing cumulonimbus clouds, *J. Geophys. Res. Atmos.*, *118*, 6580–6592, doi:10.1002/jgrd.50485.

Mattos, E. V. (2015), Relationship between polarimetric radar signatures and electrical activity in thunderstorms, PhD thesis, Cent. for Weather Forecast. and Clim. Res., Natl. Inst. for Space Res., Sao Jose dos Campos, Sao Paulo, Brazil.

Mattos, E. V., and L. A. T. Machado (2011), Cloud-to-ground lightning and mesoscale convective systems, *Atmos. Res.*, *99*, 377–390, doi:10.1016/j.atmosres.2010.11.007.

Mecikalski, R. M., A. L. Bain, and L. D. Carey (2015), Radar and lightning observations of deep moist convection across northern Alabama during DC3: 21 May 2012, *Mon. Weather Rev.*, *143*, 2774–2794, doi:10.1175/MWR-D-14-00250.1.

Metcalf, J. I. (1993), Radar observations of the effects of changing electric fields of thunderstorms, *Bull. Am. Meteorol. Soc.*, *74*, 1080–1083.

Metcalf, J. I. (1995), Radar observations of changing orientations of hydrometeors in thunderstorms, *J. Appl. Meteorol.*, *34*, 757–772, doi:10.1175/1520-0450(1995)034,0757:ROOCOO.2.0.CO;2.

Metcalf, J. I. (1997), Temporal and spatial variations of hydrometeor orientations in thunderstorms, *J. Appl. Meteorol.*, *36*, 315–321, doi:10.1175/1520-0450(1997)036,0315:TASVOH.2.0.CO;2.

Park, H. S., A. V. Ryzhkov, D. S. Zrnic, and K.-Y. Kim (2009), The hydrometeor classification algorithm for the polarimetric WSR-88D: Description and application to an MCS, *Weather Forecast.*, *24*, 730–748, doi:10.1175/2008WAF2222205.1.

Payne, C. D., T. J. Schuur, D. R. MacGorman, M. I. Biggerstaff, K. M. Kuhlman, and W. D. Rust (2010), Polarimetric and electrical characteristics of a lightning ring in a supercell storm, *Mon. Weather Rev.*, *138*, 2405–2425, doi:10.1175/2009MWR3210.1.

Petersen, W. A., and S. A. Rutledge (1998), On the relationships between cloud-to-ground lightning and convective rainfall, *J. Geophys. Res.*, *103*, 14,025–14,040, doi:10.1029/97JD02064.

Picca, J. C., M. R. Kumjian, and A. V. Ryzhkov (2010), Z_{DR} columns as a predictive tool for hail growth and storm evolution, paper presented at 25th Conference on Severe Local Storms, Am. Meteorol. Soc., Denver, Colo.

Qie, X., R. Zhu, T. Yuan, X. Wu, W. Li, and D. Liu (2014), Application of total-lightning data assimilation in a mesoscale convective system based on the WRF model, *Atmos. Res.*, *145-146*, 255–266, doi:10.1016/j.atmosres.2014.04.012.

Reynolds, S. E., M. Brook, and M. F. Gourley (1957), Thunderstorm charge separation, *J. Meteorol.*, *14*, 426–436, doi:10.1175/1520-0469(1957)014<0426:TCS>2.0.CO;2.

Rison, W., R. J. Thomas, P. R. Krehbiel, T. Hamlin, and J. Harlin (1999), A GPS-based three-dimensional lightning mapping system: Initial observations in central New Mexico, *Geophys. Res. Lett.*, *26*, 3573–3576, doi:10.1029/1999GL010856.

Rutledge, S. A., E. R. Williams, and T. D. Keenan (1992), The Down Upper Doppler and Electricity Experiment (DUNDEE): Overview and preliminary results, *Bull. Am. Meteorol. Soc.*, *73*, 3–16, doi:10.1175/1520-0477(1992)073<0003:TDUDAE>2.0.CO;2.

Ryzhkov, A. V., and D. S. Zrnic (2005), Radar polarimetry at S, C, and X bands: Comparative analysis and operational implications, paper presented at 32nd Conference on Radar Meteorology, Am. Meteorol. Soc., Norman, Okla.

Sakuragi, J., and T. Biscaro (2012), Determination of Z_{DR} offset and their impact in the hydrometeor classification, paper presented at XVII Brazilian Meteorological Conference, Braz. Meteorol. Soc., Gramado, RS, Brazil.

Saunders, C. P. R., H. Bax-Norman, C. Emersic, E. E. Avila, and N. E. Castellano (2006), Laboratory studies of the effect of cloud conditions on graupel/crystal charge transfer in thunderstorm electrification, *Q. J. R. Meteorol. Soc.*, *132*, 2653–2673, doi:10.1256/qj.05.218.

Schneebeli, M., J. Sakuragi, T. Biscaro, C. F. Angelis, I. C. da Costa, C. Morales, L. Baldini, and L. A. T. Machado (2012), Polarimetric X-band weather radar measurements in the tropics: Radome and rain attenuation correction, *Atmos. Meas. Tech.*, *5*, 2183–2199, doi:10.5194/amt-5-2183-2012.

Schultz, C. J., W. A. Petersen, and L. D. Carey (2009), Preliminary development and evaluation of lightning jump algorithms for the real-time detection of severe weather, *J. Appl. Meteorol.*, *48*, 2543–2563, doi:10.1175/2009JAMC2237.1.

Schultz, C. J., W. A. Petersen, and L. D. Carey (2011), Lightning and severe weather: A comparison between total and cloud-to-ground lightning trends, *Weather Forecast.*, *26*, 744–755, doi:10.1175/WAF-D-10-05026.1.

Schultz, C. J., L. D. Carey, E. V. Schultz, and R. J. Blakeslee (2015), Insight into the kinematic and microphysical processes that control lightning jumps, *Weather Forecast.*, *30*, 1591–1621, doi:10.1175/WAF-D-14-00147.1.

Schultz, E. V., C. J. Schultz, L. D. Carey, D. J. Cecil, and M. Bateman (2016), Automated storm tracking and the lightning jump algorithm using GOES-R Geostationary Lightning Mapper (GLM) proxy data, *J. Oper. Meteorol.*, *4*, 92–107, doi:10.15191/nwajom.2016.0407.

Snyder, J. C., H. B. Bluestein, G. Zhang, and S. J. Frasier (2010), Attenuation correction and hydrometeor classification of high-resolution, X-band, dual-polarized mobile radar measurements in severe convective storms, *J. Atmos. Oceanic Technol.*, *27*, 1979–2001, doi:10.1175/2010JTECHA1356.1.

Soula, S. (2009), Lightning and precipitation, in *Lightning: Principles, Instruments and Applications*, edited by H. D. Betz et al., pp. 447–463, Springer, Dordrecht, Netherlands, doi:10.1007/978-1-4020-9079-0_20.

Straka, J. M., D. S. Zrnić, and A. V. Ryzhkov (2000), Bulk hydrometeor classification and quantification using polarimetric radar data: Synthesis of relations, *J. Appl. Meteorol.*, *39*, 1341–1372, doi:10.1175/1520-0450(2000)039<1341:BHCAQU>2.0.CO;2.

Stuhlmann, R., A. Rodriguez, S. Tjemkes, J. Grandell, A. Arriaga, J.-L. Bézy, D. Aminou, and P. Bensi (2005), Plans for EUMETSAT's Third Generation Meteosat geostationary satellite programme, *Adv. Space Res.*, *36*, 975–981, doi:10.1016/j.asr.2005.03.091.

Takahashi, T. (1978), Riming electrification as a charge generation mechanism in thunderstorms, *J. Atmos. Sci.*, *35*, 1536–1548, doi:10.1175/1520-0469(1978)035<1536:REAACG>2.0.CO;2.

Tessendorf, S. A., S. A. Rutledge, and K. C. Wiens (2007), Radar and lightning observations of normal and inverted polarity multicellular storms from STEPS, *Mon. Weather Rev.*, *135*, 3682–3706, doi:10.1175/2007MWR1954.1.

Testud, J., E. L. Erwan, E. Obligis, and M. Ali-Mehenni (2000), The rain profiling algorithm applied to polarimetric weather radar, *J. Atmos. Oceanic Technol.*, *17*, 332–356, doi:10.1175/1520-0426(2000)017<0332:TRPAAT>2.0.CO;2.

Thomas, R. J., P. R. Krehbiel, W. Rison, T. Hamlin, J. Harlin, and D. Shown (2001), Observations of VHF source powers radiated by lightning, *Geophys. Res. Lett.*, *28*, 143–146, doi:10.1029/2000GL011464.

Thomas, R. J., P. R. Krehbiel, W. Rison, S. J. Hunyady, W. P. Winn, T. Hamlin, and J. Harlin (2004), Accuracy of the lightning mapping array, *J. Geophys. Res.*, *109*, D14207, doi:10.1029/2004JD004549.

Ventura, J. F., F. Honoré, and P. Tabary (2013), X-band polarimetric weather radar observations of a hailstorm, *J. Atmos. Oceanic Technol.*, *30*, 2143–2151, doi:10.1175/JTECH-D-12-00243.1.

Wang, N., K. Gopalan, and R. I. Albrecht (2012), Application of lightning to passive microwave convective and stratiform partitioning in passive microwave rainfall retrieval algorithm over land from TRMM, *J. Geophys. Res.*, *117*, D23203, doi:10.1029/2012JD017812.

Weinheimer, A. J., and A. A. Few (1987), The electric field alignment of ice particles in thunderstorms, *J. Geophys. Res.*, *92*, 14,833–14,844, doi:10.1029/JD092iD12p14833.

Wiens, K. C., S. A. Rutledge, and S. A. Tessendorf (2005), The 29 June 2000 supercell observed during STEPS. Part II: Lightning and charge structure, *J. Atmos. Sci.*, *62*, 4151–4177, doi:10.1175/JAS3615.1.

Williams, E. R. (1989), The tripole structure of thunderstorms, *J. Geophys. Res.*, *94*, 13,151–13,167, doi:10.1029/JD094iD11p13151.

Williams, E. R. (2006), Problems in lightning physics-the role of polarity asymmetry, *Plasma Sources Sci. Technol.*, *15*, S91–S108, doi:10.1088/0963-0252/15/2/S12.

Xu, W., R. F. Adler, and N. Wang (2013), Improving geostationary satellite rainfall estimates using lightning observations: Underlying lightning–rainfall–cloud relationships, *J. Appl. Meteorol.*, *52*, 213–229, doi:10.1175/JAMC-D-12-040.1.